J Neurophysiol 123: 755–772, 2020.
First published January 8, 2020; doi:10.1152/jn.00443.2019.

RESEARCH ARTICLE | *Cellular and Molecular Properties of Neurons*

Heterogeneities in intrinsic excitability and frequency-dependent response properties of granule cells across the blades of the rat dentate gyrus

Poonam Mishra and Rishikesh Narayanan
Cellular Neurophysiology Laboratory, Molecular Biophysics Unit, Indian Institute of Science, Bangalore, India

Submitted 12 July 2019; accepted in final form 7 January 2020

Mishra P, Narayanan R. Heterogeneities in intrinsic excitability and frequency-dependent response properties of granule cells across the blades of the rat dentate gyrus. *J Neurophysiol* 123: 755–772, 2020. First published January 8, 2020; doi:10.1152/jn.00443.2019.—The dentate gyrus (DG), the input gate to the hippocampus proper, is anatomically segregated into three different sectors, namely, the suprapyramidal blade, the crest region, and the infrapyramidal blade. Although there are well-established differences between these sectors in terms of neuronal morphology, connectivity patterns, and activity levels, differences in electrophysiological properties of granule cells within these sectors have remained unexplored. Here, employing somatic whole cell patch-clamp recordings from the rat DG, we demonstrate that granule cells in these sectors manifest considerable heterogeneities in their intrinsic excitability, temporal summation, action potential characteristics, and frequency-dependent response properties. Across sectors, these neurons showed positive temporal summation of their responses to inputs mimicking excitatory postsynaptic currents and showed little to no sag in their voltage responses to pulse currents. Consistently, the impedance amplitude profile manifested low-pass characteristics and the impedance phase profile lacked positive phase values at all measured frequencies and voltages and for all sectors. Granule cells in all sectors exhibited class I excitability, with broadly linear firing rate profiles, and granule cells in the crest region fired significantly fewer action potentials compared with those in the infrapyramidal blade. Finally, we found weak pairwise correlations across the 18 different measurements obtained individually from each of the three sectors, providing evidence that these measurements are indeed reporting distinct aspects of neuronal physiology. Together, our analyses show that granule cells act as integrators of afferent information and emphasize the need to account for the considerable physiological heterogeneities in assessing their roles in information encoding and processing.

NEW & NOTEWORTHY We employed whole cell patch-clamp recordings from granule cells in the three subregions of the rat dentate gyrus to demonstrate considerable heterogeneities in their intrinsic excitability, temporal summation, action potential characteristics, and frequency-dependent response properties. Across sectors, granule cells did not express membrane potential resonance, and their impedance profiles lacked inductive phase leads at all measured frequencies. Our analyses also show that granule cells manifest class I excitability characteristics, categorizing them as integrators of afferent information.

Address for reprint requests and other correspondence: R. Narayanan, Molecular Biophysics Unit, Indian Inst. of Science, Bangalore 560 012, India (e-mail: rishi@iisc.ac.in).

excitability; heterogeneities; hippocampus; impedance; temporal summation

INTRODUCTION

The dentate gyrus (DG), the input gate to the mammalian hippocampus proper (Amaral et al. 2007; Andersen et al. 2006), has been implicated in spatial navigation, response decorrelation, pattern separation, and engram formation. Granule cells are the prominent neuronal subtype within the DG and have been studied extensively from the perspective of their intrinsic response properties, plasticity profiles, in vivo response properties, role as engram cells, sparse connectivity and sparse firing characteristics, and neurogenesis (Aimone et al. 2014; Amaral et al. 2007; Bakker et al. 2008; Bliss and Lomo 1973; Danielson et al. 2017; Diamantaki et al. 2016; Good-Smith et al. 2017; Heigele et al. 2016; Kropff et al. 2015; Leutgeb et al. 2007; Li et al. 2017; McHugh et al. 2007; Mishra and Narayanan 2019; Neunuebel and Knierim 2014; Sahay et al. 2011; Senzai and Buzsáki 2017; Tonegawa et al. 2018). Electrophysiological recordings from granule cells have been employed to evaluate their response characteristics, including assessments of important differences between mature and immature cell excitability (Fricke and Prince 1984; Krueppel et al. 2011; Liu et al. 1996; Mody et al. 1992; Pedroni et al. 2014; Schmidt-Hieber et al. 2004; 2007; Staley et al. 1992; van Praag et al. 2002). The DG, within each location along its dorsoventral span, is anatomically segregated into three different sectors: the suprapyramidal blade, the crest region, and the infrapyramidal blade (Amaral et al. 2007). There are several well-established differences across these three sectors (Amaral et al. 2007), including morphological differences (Claiborne et al. 1990; Desmond and Levy 1982, 1985; Gallitano et al. 2016; Green and Juraska 1985; Schneider et al. 2014), connectivity patterns (Claiborne et al. 1986), the ratio of basket cells to granule cells (Seress and Pokorny 1981), and activity levels (Chawla et al. 2005; Marrone et al. 2012a, 2012b; Ramirez-Amaya et al. 2006, 2013; Ramírez-Amaya et al. 2005; Satvat et al. 2012). Despite this, differences in electrophysiological properties of granule cells present within these sectors have surprisingly remained unexplored. In addition, as the DG is present within an oscillatory network (Bland 1986; Buzsáki 2002; Colgin 2013, 2016; Sainsbury and Bland 1981; Winson 1974, 1978), it is important that neuronal response properties are assessed in a frequency-dependent manner, rather than

  ISSN 0022-3077.

being confined to steady-state measures of subthreshold excitability (Cole 1941; Cole and Baker 1941a, 1941b; Das et al. 2017; Hu et al. 2002; Hutcheon and Yarom 2000; Krueppel et al. 2011; Mauro et al. 1970; Narayanan and Johnston 2007, 2008; Pike et al. 2000; Schmidt-Hieber et al. 2007; Stegen et al. 2012). The frequency-dependent response characteristics of DG granule cells, however, have also not been systematically characterized across these three DG sectors.

To fill these lacunae, in this study we performed patch-clamp electrophysiological recordings of granule cells from the three sectors of the rat DG and systematically measured their electrophysiological characteristics. We show that the granule cells in these different DG sectors manifest considerable heterogeneities in their intrinsic excitability, temporal summation, action potential (AP) characteristics, and frequency-dependent response properties. We found that the subthreshold excitability measures were dependent on membrane voltage, with significant hyperpolarization-induced reduction in the gain of granule cells across all sectors. Across sectors, these neurons showed positive temporal summation of their responses to current injections that mimicked excitatory postsynaptic currents (EPSCs) and showed little to no sag in their voltage responses to hyperpolarizing or depolarizing pulse current injections. Consistently, the impedance amplitude profile manifested low-pass characteristics and the impedance phase profile distinctly lacked positive phase values at all measured frequencies and voltages and for all DG sectors.

Granule cells across the three DG sectors exhibited class I excitability, where they were able to fire APs at arbitrarily low firing rates, with broadly linear profiles of firing rate vs. current injection (*f–I*) curves. Together, the low-pass frequency-response characteristics, the lack of positive impedance phase, and the linear *f–I* curve showing class I excitability point to DG neurons across all these sectors acting as integrators of afferent information. We found no significant differences in subthreshold response properties of these neurons across the three DG sectors. However, we found that granule cells in the crest region fired fewer APs, in response to suprathreshold current injections, compared with their counterparts in the infrapyramidal blade. Finally, we assessed correlations across the 18 different sub- and suprathreshold measurements for each of the three DG sectors and found a large number of measurement pairs showing weak pairwise correlations. This large subset of uncorrelated measurements suggested that the set of measurements employed here in characterizing DG granule cells are assessing distinct aspects of their physiology. Together, our analyses show that DG neurons act as integrators of afferent information and emphasize the need to account for the considerable heterogeneities inherent to this population of neurons in assessing their physiology, including engram formation and their ability to perform channel and pattern decorrelation.

MATERIALS AND METHODS

Ethical approval. All experiments reported in this study were reviewed and approved by the Institute Animal Ethics Committee of the Indian Institute of Science, Bangalore. Experimental procedures were similar to previously established protocols (Ashhad et al. 2015; Ashhad and Narayanan 2016; Das and Narayanan 2017; Narayanan et al. 2010; Narayanan and Johnston 2007, 2008; Rathour et al. 2016) and are detailed below. Animals were provided ad libitum food and water and were housed with an automated 12:12-h light-dark cycle, with the facility temperature maintained at 21 ± 2°C. All animals were obtained from the in-house breeding setup at the central animal facility of the Indian Institute of Science.

Slice preparation for in vitro patch-clamp recording. Electrophysiological recordings (from a total of ~200 neurons) reported in this study were obtained from 66 male Sprague-Dawley rats of 6- to 8-wk age, with ~96% recordings from rats in the 7–8 wk age group. Rats were anesthetized by intraperitoneal injection of a ketamine-xylazine mixture. After onset of deep anesthesia, assessed by cessation of toe-pinch reflex, transcardial perfusion of ice-cold cutting solution was performed. The cutting solution contained (in mM) 2.5 KCl, 1.25 NaH_2PO_4, 25 $NaHCO_3$, 0.5 $CaCl_2$, 7 $MgCl_2$, 7 dextrose, 3 sodium pyruvate, and 200 sucrose (pH 7.3, ~300 mosM) saturated with 95% O_2-5% CO_2. Thereafter, the brain was removed quickly and 350-μm-thick near-horizontal slices were prepared from middle hippocampi (bregma, −6.5 mm to −5.1 mm) with a vibrating blade microtome (Leica Vibratome) while submerged in ice-cold cutting solution saturated with 95% O_2-5% CO_2. The slices were then incubated for 10–15 min at 34°C in a chamber containing a holding solution (pH 7.3, ~300 mosM) with the composition of (in mM) 125 NaCl, 2.5 KCl, 1.25 NaH_2PO_4, 25 $NaHCO_3$, 2 $CaCl_2$, 2 $MgCl_2$, 10 dextrose, and 3 sodium pyruvate saturated with 95% O_2-5% CO_2. Thereafter, the slices were kept in a holding chamber at room temperature for at least 45 min before the start of recordings. A maximum of six middle hippocampal slices were obtained from each rat, and a maximum of two neuronal recordings were obtained from each slice.

Electrophysiology: whole cell current-clamp recording. For electrophysiological recordings, slices were transferred to the recording chamber and continuously perfused with carbogenated artificial cerebrospinal fluid (ACSF-extracellular recording solution) at a flow rate of 2–3 mL/min. All neuronal recordings were performed under current-clamp configuration at physiological temperatures (32–35°C) achieved through an inline heater that was part of a closed-loop temperature control system (Harvard Apparatus). The carbogenated ACSF contained (in mM) 125 NaCl, 3 KCl, 1.25 NaH_2PO_4, 25 $NaHCO_3$, 2 $CaCl_2$, 1 $MgCl_2$, and 10 dextrose (pH 7.3; ~300 mosM). Slices were first visualized under a ×10 objective lens to locate the granule cell layer of the DG, and then a ×63 water-immersion objective lens was employed to perform patch-clamp recordings from DG granule cells, through a Dodt contrast microscope (Carl Zeiss Axioexaminer). Whole cell current-clamp recordings were performed from visually identified DG granule cell somata with Dagan BVC-700A amplifiers.

Borosilicate glass electrodes with electrode tip resistance between 2 and 6 MΩ (more often electrodes with ~4-MΩ tip resistance were used) were pulled (P-97 Flaming/Brown micropipette puller; Sutter) from thick glass capillaries (1.5-mm outer diameter and 0.86-mm inner diameter; Sutter) and used for patch-clamp recordings. The pipette solution contained (in mM) 120 K-gluconate, 20 KCl, 10 HEPES, 4 NaCl, 4 Mg-ATP, 0.3 Na-GTP, and 7 K_2-phosphocreatine (pH 7.3 adjusted with KOH; osmolarity ~300 mosM). Series resistance was monitored and compensated online with the bridge-balance circuit of the amplifier. Experiments were discarded only if the initial resting membrane potential was more depolarized than −60 mV and if series resistance rose above 30 MΩ or if there were fluctuations in temperature and ACSF flow rate during the course of the experiment. Unless otherwise stated, experiments were performed at the initial resting membrane potential (reported here as V_{RMP}) of the cell. Voltages have not been corrected for the liquid junction potential, which was experimentally measured to be ~8 mV.

Subthreshold measurements. We characterized DG granule neurons with several electrophysiological measurements obtained through pulse-current and frequency-dependent current injections (Ashhad et al. 2015; Ashhad and Narayanan 2016; Das and Narayanan 2017; Malik et al. 2016; Mishra and Narayanan 2019; Narayanan et al. 2010; Narayanan and Johnston 2007, 2008; Rathour et al. 2016). Input resistance (R_{in}) was measured as the slope of a linear fit to the

steady-state voltage-current (*V-I*) plot obtained by injecting subthreshold current pulses of amplitudes spanning –50 to +50 pA, in steps of 10 pA (Fig. 1*A*). Owing to very high R_{in} of many cells, and to avoid spike generation for positive current injections, we also performed recordings in response to –25 to +25 pA current injection, in steps of 5 pA. To assess temporal summation, five α-excitatory postsynaptic potentials (α-EPSPs) with 50-ms interval were evoked by current injections of the form $I_\alpha = I_{max}\, t \exp(-\alpha t)$, with $\alpha = 0.1\ ms^{-1}$ (Fig. 1*B*). Temporal summation ratio (S_α) in this train of five EPSPs was computed as E_{last}/E_{first}, where E_{last} and E_{first} are the amplitudes of the last and first EPSPs in the train, respectively. Percentage sag was measured from the voltage response of the cell to a hyperpolarizing current pulse of 100 pA and was defined as $100\,(1 - V_{ss}/V_{peak})$, where V_{ss} and V_{peak} depict the steady-state and peak voltage deflection from V_{RMP}, respectively.

The chirp stimulus (Fig. 1*C*) used for characterizing the impedance amplitude (ZAP) and phase (ZPP) profiles was a sinusoidal current of constant amplitude below firing threshold, with its frequency linearly spanning 0–15 Hz in 15 s (*Chirp15*). The voltage response of the neuron was recorded for *Chirp15* current stimulus injection at V_{RMP} and for various voltage values (Fig. 1*D*). The magnitude of the ratio of the Fourier transform of the voltage response to the Fourier transform of the *Chirp15* stimulus formed the impedance amplitude profile (Fig, 1*E*). The frequency at which the impedance amplitude reached its maximum was the resonance frequency (f_R). Resonance strength (Q) was measured as the ratio of the maximum impedance amplitude to the impedance amplitude at 0.5 Hz (Hu et al. 2002). Total inductive phase (Φ_L) was defined as the area under the inductive part of the ZPP (Narayanan and Johnston 2008). A 100-pA hyperpolarizing current pulse was provided before the chirp current (Fig. 1*C*) to estimate input

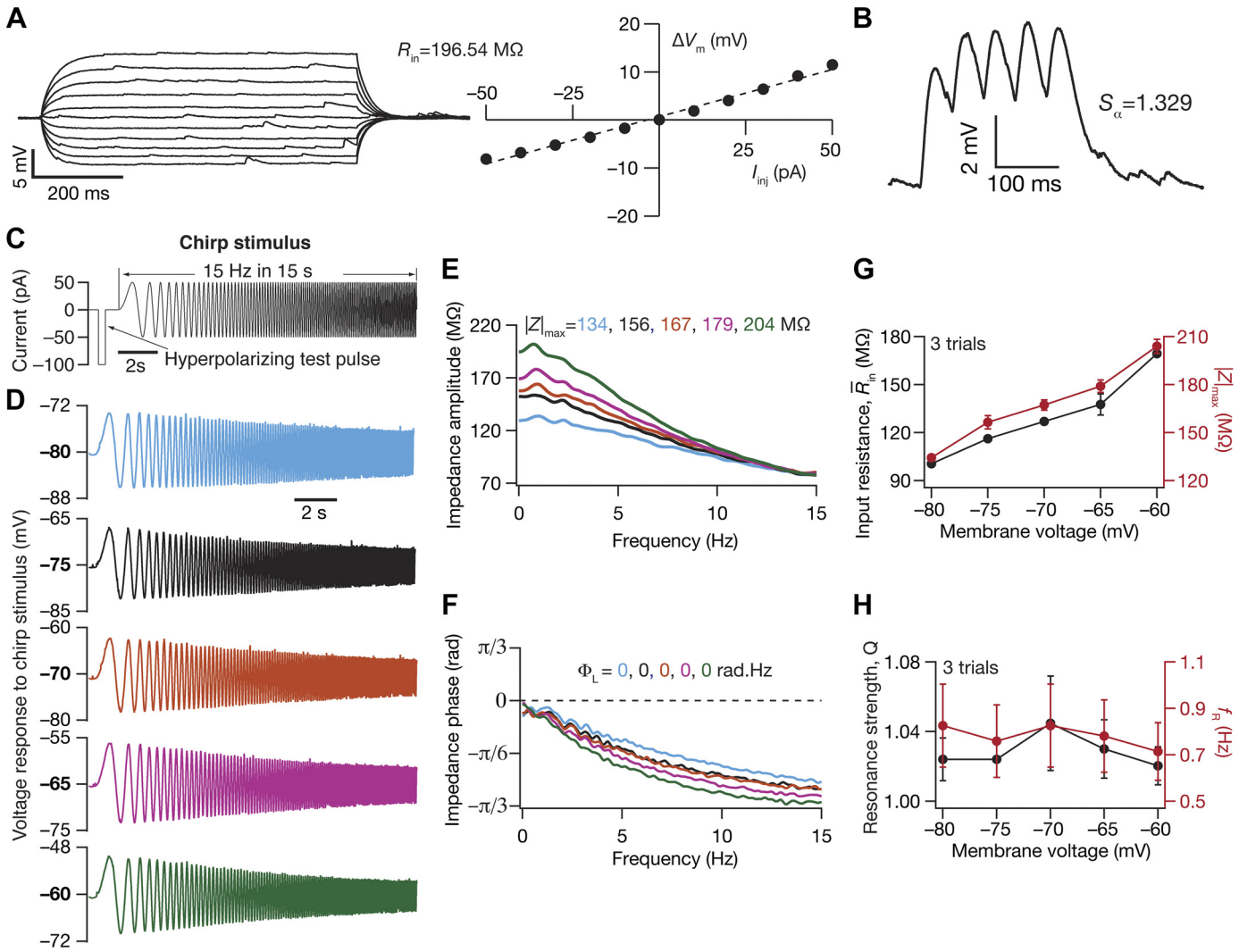

Fig. 1. Electrophysiological protocols and measurements employed in the characterization of subthreshold excitability and frequency-dependent response properties of dentate gyrus granule cells. *A*, *left*: voltage responses of an example neuron to 700-ms current pulses of amplitude varying from –50 pA to +50 pA (in steps of 10 pA). *Right*: input resistance (R_{in}) was calculated as the slope of the plot depicting steady-state voltage response (ΔV_m) as a function of the injected current amplitude (I_{inj}). *B*: voltage response of the example neuron to 5 α-current injections arriving at 20 Hz, depicting temporal summation. Temporal summation ratio (S_α) was computed as the ratio of the amplitude of the 5th response to that of the 1st. *C*: chirp stimulus employed for assessing frequency-dependent response properties of the dentate gyrus granule cells. The chirp stimulus employed here was a sinusoidal current of constant amplitude, with frequency varying linearly from 0 to 15 Hz over a 15-s period. A 100-pA hyperpolarizing current pulse was provided before the chirp current to estimate input resistance ($\bar{R}_{in}$) and to observe and correct series resistance changes through the course of the experiment. *D*: voltage responses of the example neuron to the chirp current at different voltages. The color code for voltages here continues in *E* and *F*. *E* and *F*: impedance amplitude (*E*) and phase (*F*) profiles computed from the current stimulus shown in *C* and the voltage responses shown in *D*. $|Z|_{max}$, the maximum impedance amplitude; Φ_L, the total inductive phase. *G*: $\bar{R}_{in}$ from a single hyperpolarizing pulse (*C*) and $|Z|_{max}$ (*D*) plotted as functions of the membrane voltage at which the chirp stimulus responses were measured. *H*: resonance strength (Q) and resonance frequency (f_R) plotted as functions of the membrane voltage at which the chirp stimulus responses were measured.

resistance ($\bar{R}_{in}$) and to observe and correct series resistance changes through the course of the experiment.

To characterize these subthreshold physiological measurements (see Table 1) of granule cells, recordings were performed at V_{RMP} from the three major well-defined sectors of DG (Fig. 2): suprapyramidal blade, crest region, and infrapyramidal blade (Amaral et al. 2007). The boundaries between these three regions were identified visually from the curvature of the granule cell layer (Amaral et al. 2007). Specifically, cells recorded from the semicircular region between the two flat blades were assigned to the "crest region," the flat blade closer to CA1 was called the "suprapyramidal blade," and the one farther away from CA1 was referred to as the "infrapyramidal blade" (Fig. 2*A*). The recordings were uniformly distributed within the granule cell layer, across deep, superficial, and medial regions (along the hilus-molecular layer axis), of these sectors. Images of cell location were stored for post facto classification into one of three granule cell sectors. The characterization protocol to measure subthreshold measurements was repeated for a range of membrane voltages in a subset of cells, to assess the dependence of these measurements on membrane voltage (Fig. 1, *D–H*; Fig. 3).

Suprathreshold measurements. Action potential (AP) firing frequency was computed by extrapolating the number of spikes obtained during a 700-ms current injection to 1 s (Fig. 4*A*). Current amplitude of these pulse current injections was varied from 0 pA to 250 pA in steps of 50 pA, to construct the firing frequency vs. injected current (*f–I*) plot (Fig. 4*B*). Various AP-related measurements (Malik et al. 2016; Mishra and Narayanan 2019) were derived from the voltage response of the cell to a 250-pA pulse current injection (Fig. 4, *C* and *D*). AP amplitude (V_{AP}) was computed as the difference between the peak voltage of the spike (V_{AP}^{peak}) and V_{RMP} (Fig. 4*C*). The temporal distance between the timing of the first spike and the time of current injection was defined as latency to first spike (T_{1AP}; Fig. 4*C*). The duration between the first and the second spikes was defined as the first interspike interval (T_{1ISI}; Fig. 4*C*). AP half-width (T_{APHW}; Fig. 4*D*) was the temporal width measured at the half-maximal points of the AP peak with reference to V_{RMP}. The maximum $\left(\frac{dV}{dt}\Big|_{AP}^{max}\right)$ and minimum $\left(\frac{dV}{dt}\Big|_{AP}^{min}\right)$ values of the AP temporal derivative were calculated from the temporal derivative of the AP trace (Fig. 4*D*). The voltage in the AP trace corresponding to the time point at which the dV/dt crossed 20 V/s defined AP threshold (Fig. 4*D*). All suprathreshold measurements were obtained through current injections into the cell resting at V_{RMP} and were measured across each of the three sectors of the DG (Figs. 5 and 6).

Statistical analyses. To assess pairwise relationship in 18 different sub- and suprathreshold measurements, we analyzed the scatterplot matrices of these measurements individually from each of the three sectors (Fig. 7, *A–C*) as well of pooled measurements for all three sectors (Fig. 7*D*). We computed Pearson's correlation coefficients (R), and corresponding significance values (P), for each of these pairwise scatterplots and analyzed the distribution of correlation coefficients for each population (Fig. 7). Qualitative descriptions about weak vs. strong correlations were adopted from the definitions in the literature, with reference to the value of R (Evans 1996).

All data acquisition and analyses were performed with custom-written software in IGOR Pro (WaveMetrics), and statistical analyses were performed with the R computing package (http://www.r-project.org/). Across figures, the statistics employed for data presentation was consistent with the statistical test used to compare two populations of data. Specifically, when data are reported as means ± SE, parametric tests (ANOVA followed by Tukey's honestly significant difference test, Student's t test) were employed, and when data are reported as median (along with the entire distribution of the data or the quartiles), we employed nonparametric tests (Kruskal–Wallis, Wilcoxon rank sum). To emphasize the heterogeneities, we have reported all data points, and not just the statistics behind the data to avoid misinterpretations arising from reporting of summary statistics (Marder and Taylor 2011; Rathour and Narayanan 2019). In addition, we employed three standard measures of degree of variability to quantify heterogeneity in individual measurements: standard deviation, interquartile range, and coefficient of variation. Wherever possible, results of both parametric and nonparametric statistical tests are provided either in the figures or in the legends.

RESULTS

In assessing the intrinsic response properties of DG granule cells across its different blades, we performed patch-clamp electrophysiological recordings in current-clamp mode at the cell body of visually identified granule cells. We first characterized the response properties of these neurons with a range of subthreshold electrophysiological measurements (Fig. 1). We measured input resistance from the steady-state voltage re-

Table 1. *Subthreshold measurements when respective current stimuli were injected with cell resting at V_{RMP}*

Measurement	Symbol	Suprapyramidal Blade	Crest Region	Infrapyramidal Blade
Resting membrane potential, mV	V_{RMP}	−74.69 ± 0.68 (41); 4.35; 4.76; –0.058	−76.09 ± 0.49 (74); 4.22; 4.08; –0.055	−75.26 ± 0.38 (85); 3.52; 4.02; –0.046
Input resistance, MΩ	R_{in}	174.44 ± 14.73 (41); 94.29; 85.65; 0.54	157.22 ± 6.51 (74); 56.02; 64.76; 0.35	179.44 ± 7.84 (85); 72.25; 76.42; 0.40
Temporal summation ratio	S_α	1.36 ± 0.05 (25); 0.24; 0.25; 0.17	1.33 ± 0.02 (57); 0.14; 0.18; 0.11	1.34 ± 0.02 (51); 0.17; 0.24; 0.13
Input resistance estimate, MΩ	$\bar{R}_{in}$	117.42 ± 6.82 (35); 40.34; 51.27; 0.34	118.02 ± 4.16 (73); 35.51; 35.3; 0.30	119.54 ± 4.09 (64); 32.76; 44.29; 0.27
Sag ratio	Sag	3.33 ± 0.22 (35); 1.28; 2.14; 0.38	3.08 ± 0.18 (73); 1.53; 1.47; 0.49	3.10 ± 0.20 (64); 1.60; 1.81; 0.51
Resonance frequency, Hz	f_R	0.73 ± 0.03 (35); 0.16; 0.17; 0.22	0.75 ± 0.01 (73); 0.11; 0.16; 0.15	0.74 ± 0.02 (64); 0.18; 0.23; 0.25
Maximum impedance amplitude, MΩ	$\|Z\|_{max}$	175.78 ± 13.54 (35); 80.09; 87.16; 0.45	174.48 ± 8.31 (73); 70.96; 71.8; 0.4	180.28 ± 7.97 (64); 63.77; 79.88; 0.35
Resonance strength	Q	1.03 ± 0.01 (35); 0.03; 0.03; 0.03	1.03 ± 0.003 (73); 0.02; 0.02; 0.02	1.04 ± 0.01 (64); 0.04; 0.04; 0.04
Total inductive phase, rad·Hz	Φ_L	0.011 ± 0.003 (35); 0.0172; 0.02; 1.61	0.005 ± 0.002 (71); 0.012; 0.003; 2.41	0.014 ± 0.004 (63); 0.03; 0.01; 2.172

Measurements are means ± SE (n cells), and the degree of variability in each measurement is reported as standard deviation, interquartile range, and coefficient of variation.

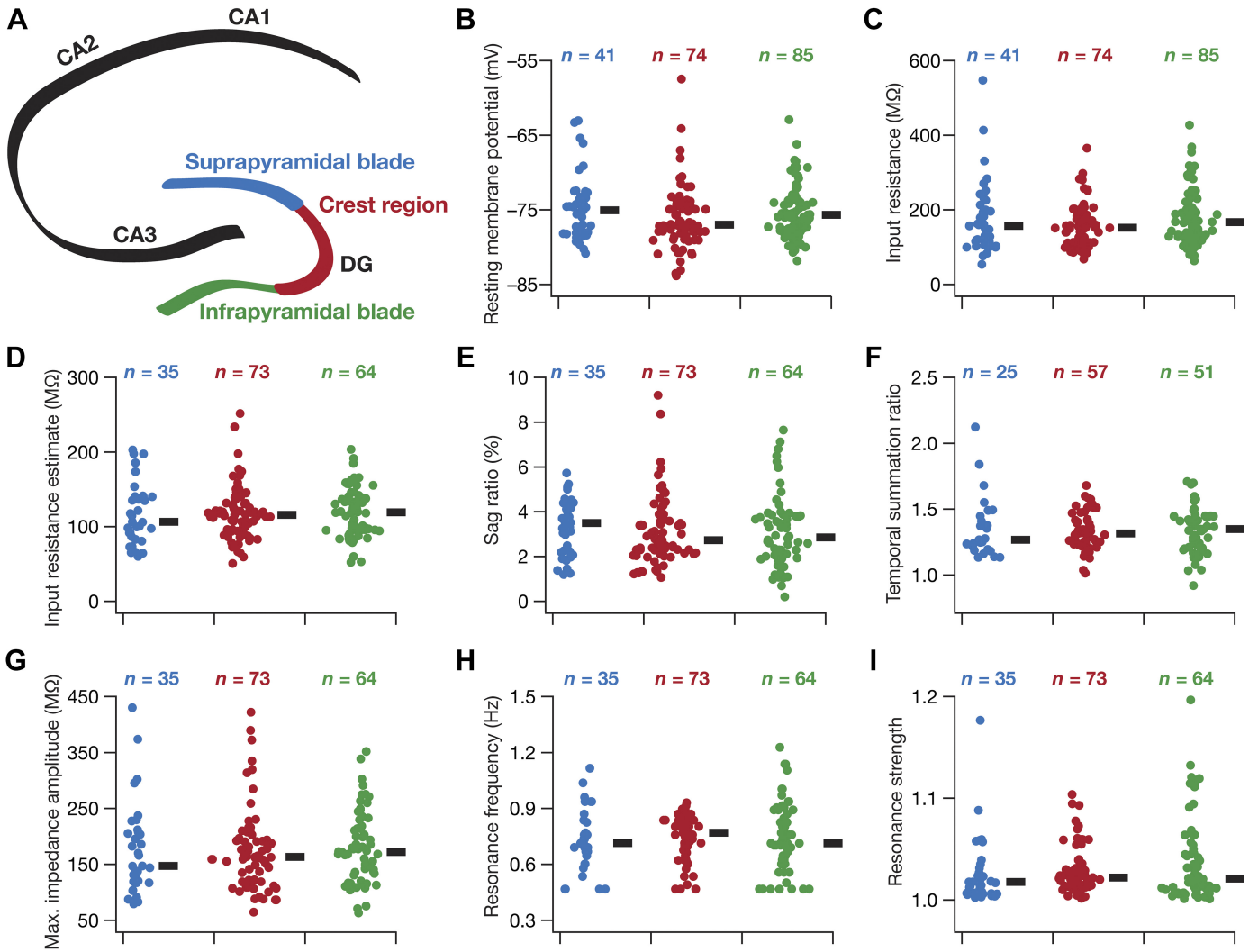

Fig. 2. Heterogeneity in subthreshold response properties of granule cells across the blades of the dentate gyrus (DG). *A*: schematic of the hippocampus proper, showing the different cornu ammonis (CA) subregions (CA1, CA2, and CA3) and the 3 sectors of the DG (infrapyramidal blade, crest region, and suprapyramidal blade). The color codes associated with the 3 DG sectors apply to *B–I*. *B–I*: beeswarm plots depicting the heterogeneous subthreshold measurements from the 3 DG sectors. The black rectangles on *right* of each beeswarm plot represent the median for the specified population. All measurements depicted in this figure were obtained through current injections into a cell resting at resting membrane potential (V_{RMP}). None of the 8 subthreshold measurements were significantly different across the 3 sectors (both Kruskal–Wallis and ANOVA tests, $P > 0.1$).

sponse to pulse current injections of different depolarizing and hyperpolarizing amplitudes (Fig. 1*A*). Input resistance, a steady-state measure of neuronal gain and excitability, is inadequate in characterizing neuronal response properties to ethologically relevant time-varying signals. Therefore, to assess neuronal response properties to time-varying signals, we injected multiple current stimuli that mimicked EPSCs into neurons to understand temporal summation properties (Magee 1998, 1999). We found considerable temporal summation of EPSPs, with the value of temporal summation ratio above unity (Fig. 1*B*).

As the DG resides in an oscillatory neural network (Bland 1986; Buzsáki 2002; Colgin 2013, 2016; Sainsbury and Bland 1981; Winson 1974, 1978), we assessed neuronal response properties to sinusoidal stimulus of different frequencies. A standard stimulus that is employed in assessing frequency-dependent response properties is the chirp current stimulus (Fig. 1*C*), which is a sinusoidal current of constant amplitude but with monotonically increasing frequency (Gimbarzevsky et al. 1984; Hutcheon and Yarom 2000; Krueppel et al. 2011; Stegen et al. 2012). We found that the frequency-dependent response profile was low pass in nature for all measured subthreshold voltages (Fig. 1, *D* and *E*), in stark contrast to the band-pass profiles of other cell types within the hippocampal formation, such as the medial entorhinal stellate neurons (Erchova et al. 2004; Giocomo et al. 2007) and CA1 pyramidal neurons (Hu et al. 2002, 2009; Narayanan and Johnston 2007, 2008; Pike et al. 2000). The gain of the system, measured as impedance amplitude, reduced especially across lower frequencies with hyperpolarization of membrane potential (Fig. 1, *D* and *E*), reflected in the maximal impedance amplitude $|Z|_{max}$ reducing with hyperpolarization (Fig. 1*E*).

The advantage of employing impedance as an excitability measure is twofold. First, impedance amplitude measures neuronal excitability as a function of input frequency, providing a frequency-dependent excitability metric, and second, impedance phase provides the temporal relationship between the voltage response and current input at various input frequencies

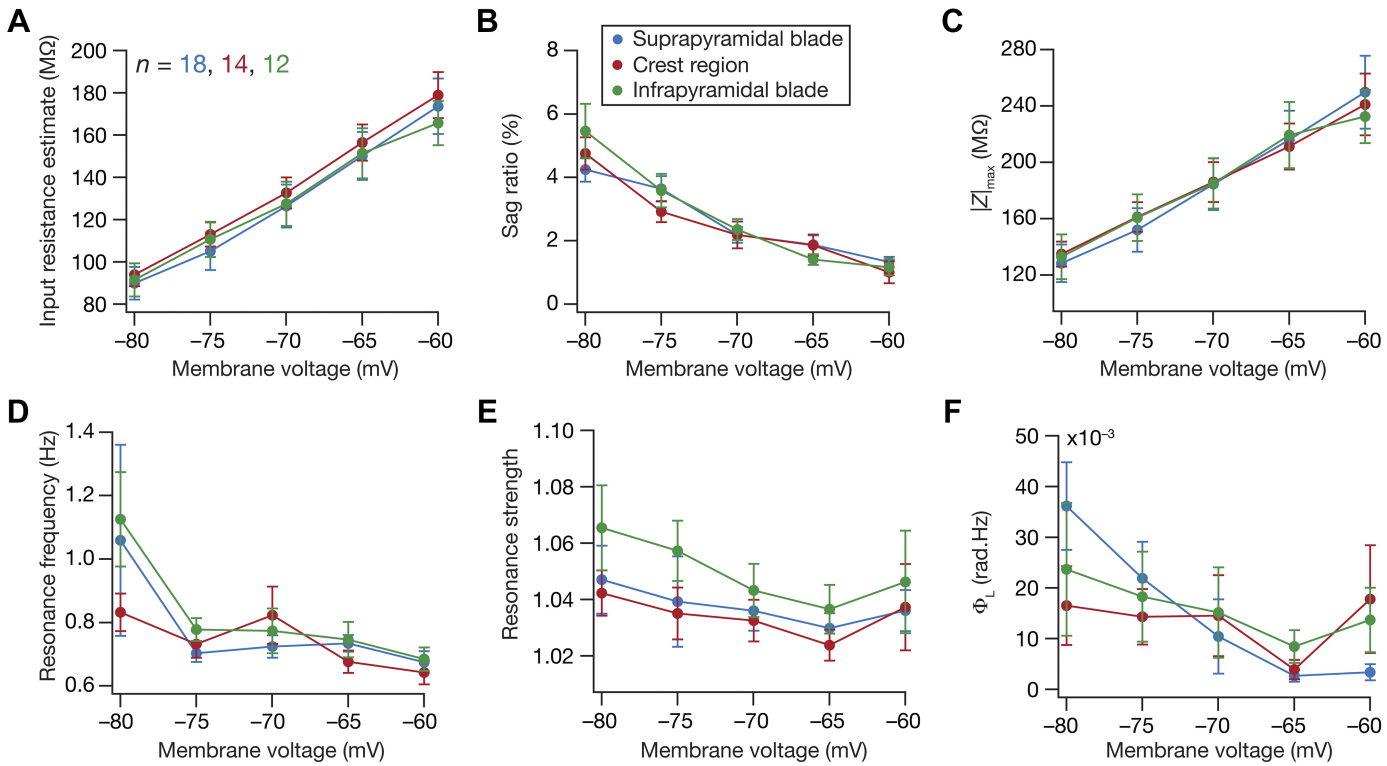

Fig. 3. Voltage dependence of subthreshold response properties of granule cells across the blades of the dentate gyrus (DG): voltage dependence of steady-state (*A* and *B*) and frequency-dependent (*C*–*F*) subthreshold measurements from the 3 DG sectors. The color codes for the 3 sectors are the same as those in Fig. 2. Refer to the text describing these results for statistical tests. $|Z|_{max}$, the maximum impedance amplitude; Φ_L, the total inductive phase.

(Mauro 1961; Mauro et al. 1970; Narayanan and Johnston 2008; Sabah and Leibovic 1969). We computed the impedance phase at all measured frequencies and found the voltage response to lag the injected current at all membrane voltages (Fig. 1*F*). This is in striking contrast with CA1 pyramidal and entorhinal stellate cells, where the impedance phase profile is biphasic, with the voltage response leading the current injection at theta-frequency range and lagging beyond theta-frequency range (Erchova et al. 2004; Mittal and Narayanan 2018; Narayanan and Johnston 2008). We also noted that the maximal lag observed at the highest measured frequency (15 Hz) reduced with increasing hyperpolarization, pointing to a systematic increase in inductive component. This increased inductive component, however, was unable to drive impedance phase values to positive ranges even in the most hyperpolarized recordings. We quantified this lack of positive impedance phase values as Φ_L, the area under the inductive (positive) part of the ZPP, which was zero at all voltages where chirp responses were recorded (Fig. 1*F*).

As functions of membrane voltage, both input resistance as well as maximal impedance amplitude reduced with hyperpolarization, indicating a reduction in overall neuronal excitability at hyperpolarized voltages (Fig. 1*G*). The resonance frequency (f_R) was <1 Hz, and the resonance strength was close to unity at all measured voltages (Fig. 1*H*), indicating low-pass response characteristics of this DG cell.

Heterogeneities in subthreshold measurements across different blades of the dentate gyrus. How do these different steady-state and frequency-dependent subthreshold measures of granule cell response vary across the different blades of the DG? To address this question, we measured the different electrophysiological properties (Fig. 1) at resting membrane potential from granule cells located within the three prominent sectors within the DG: the suprapyramidal blade, the crest region, and the infrapyramidal blade (Fig. 2*A*). First, we found considerable cell-to-cell variability in each of these response properties, spanning all three sectors (Fig. 2, *B*–*I*; Table 1). For instance, whereas the median value of input resistance was around 150 MΩ across all three sectors, the input resistance spanned a large range from tens to hundreds of megaohms (Fig. 2*C*). Second, we found that none of these subthreshold measurements was significantly different across the three sectors (Fig. 2, *B*–*I*), implying the similarity in the degree of heterogeneity across all sectors of DG. We quantified degrees of heterogeneity in each of these measurements, employing three statistical measures (standard deviation, interquartile distance, and coefficient of variation), and found them to be comparable across the three sectors (Table 1).

These measurements confirmed that DG granule cells across all three substructures lack prominent sag (Fig. 2*E*) that is characteristic of the expression of resonance. This was consistent with the resonance frequency of these neurons falling around 1 Hz (Fig. 2*H*), with the resonance strength centered on unity (Fig. 2*I*). Together, these measurements indicate that DG granule cells across all three sectors exhibited low-pass response characteristics. The temporal summation of α-current inputs showed the fifth EPSP to have higher amplitude than the first (temporal summation ratio >1) for most recorded neurons across all three sectors, indicating an enhanced temporal summation in these neurons (Fig. 2*F*). However, cells within each sector exhibited significant heterogeneity in terms of how they responded to the train of α-current inputs, with temporal

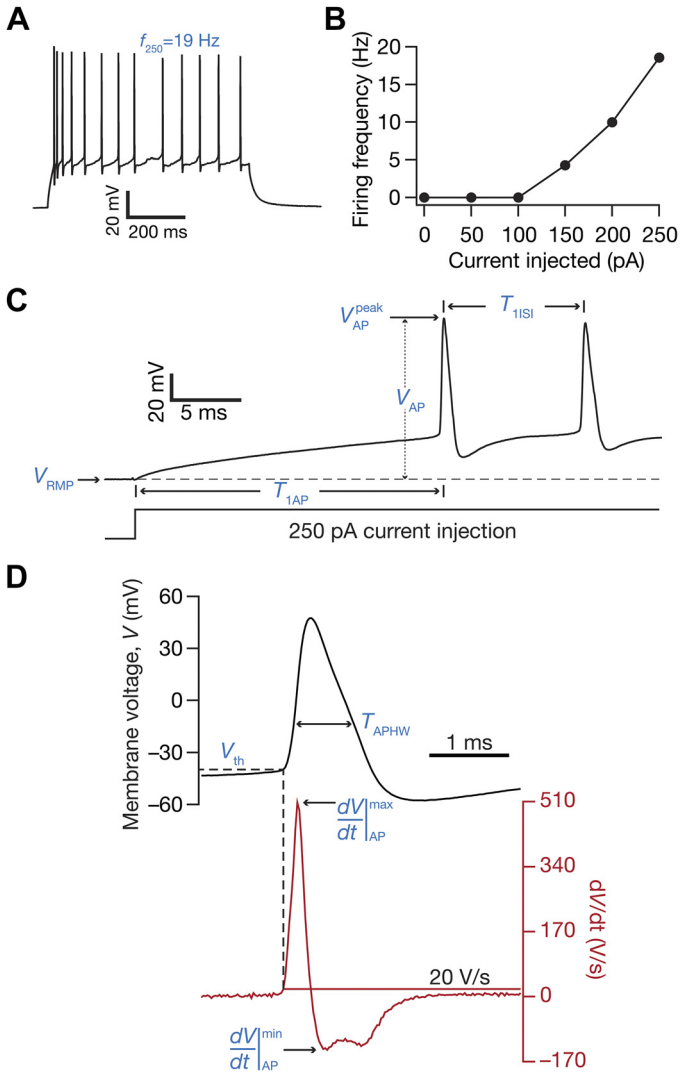

Fig. 4. Electrophysiological protocols and measurements employed in the characterization of suprathreshold excitability of dentate gyrus granule cells. *A*: voltage response of the example neuron (same neuron as Fig. 1) to a 700-ms current pulse of 250 pA (f_{250}). *B*: frequency of firing plotted as a function of injected current amplitude for the example cell shown; note that these are firing frequencies converted from the number of spikes for a 700-ms duration. *C*: zoomed version of the trace shown in *A*, illustrating electrophysiological measurements. V_{RMP}, resting membrane potential; T_{1AP}, the latency to the first action potential, measured from the time where the current injection was initiated; V_{AP}^{peak}, the maximum voltage value measured on the 1st action potential; V_{AP}, the action potential amplitude, measured as the difference between V_{AP}^{peak} and V_{RMP}; T_{1ISI}, 1st interspike interval measured as the temporal distance between the 1st and the 2nd action potentials. *D*: further zoomed version of the trace in *A* (black), along with its temporal derivative (d*V*/d*t*; red) illustrating electrophysiological measurements: the maximum $\left(\frac{dV}{dt}\Big|_{AP}^{max}\right)$ and minimum $\left(\frac{dV}{dt}\Big|_{AP}^{min}\right)$ values of the action potential temporal derivative are depicted; the value on the voltage trace at the time when the value of the action potential temporal derivative crosses 20 V/s was assigned as the action potential threshold voltage (V_{th}); the full width at half-maximum of the action potential (with the maximum given by V_{AP}) was assigned as T_{APHW}.

summation ranging from a value just lower than unity to values >1.5 in certain cells (Fig. 2*F*).

Dentate gyrus granule cells exhibited low-pass response characteristics and lacked inductive lead in their impedance phase profiles at all subthreshold voltages and across different blades. How does neuronal excitability change as a function of membrane voltage? Do these cells exhibit band-pass characteristics at more depolarized or hyperpolarized voltages, similar to the voltage-dependent resonance properties observed in CA1 pyramidal and entorhinal stellate neurons? Are there sector-specific differences in terms of how neurons respond to different voltages? To address these questions, we altered the neuronal membrane potential employing DC current injection and recorded subthreshold measurements at five different voltage values (Fig. 3). We found neuronal excitability to reduce with increased hyperpolarization, inferred from significant hyperpolarization-induced reductions in input resistance (Fig. 3*A*) and maximum impedance amplitude (Fig. 3*C*) across all three sectors. These two measures of subthreshold excitability significantly reduced with hyperpolarization in membrane voltage (ANOVA followed by Student's *t* test for each of the 10 unique pairs across the 5 voltages, $P < 0.001$) but were not significantly different across the three sectors (ANOVA, $P > 0.5$). We noted that the degree of heterogeneity in these two measurements was considerable across cells, even when measured at a specific membrane voltage. Specifically, we quantified the degree of heterogeneity with three statistical measures (standard deviation, interquartile distance, and coefficient of variation) associated with these two voltage-dependent excitability measurements (Table 2). For each of the three sectors and at all five of the voltages at which measurements were performed, we found the degree of heterogeneity in these measurements to be comparable to those observed at V_{RMP} (compare degree of heterogeneity in these measurements in Table 1 vs. Table 2). Together, these results demonstrated the voltage dependence of these two subthreshold excitability measurements, apart from providing evidence that the heterogeneity reported in Fig. 2 is not a simple reflection of the heterogeneity in V_{RMP}.

We noted that sag (Fig. 3*B*) and resonance frequency (Fig. 3*D*) did not change significantly with membrane voltages and resonance strength continued to center at unity (Fig. 3*E*). Statistically, sag, resonance frequency, resonance strength, and total inductive phase were not significantly different across sectors or across voltages (Fig. 3; ANOVA, $P > 0.5$). Furthermore, the total inductive phase was negligibly small across all voltages, confirming the absence of an inductive phase lead in the impedance profile of granule cells across all three sectors (Fig. 3*F*). Together these results demonstrated that DG granule cells exhibit low-pass response properties with a distinct absence of inductive lead in the impedance phase, at all subthreshold voltages and across the three sectors of the DG.

Heterogeneities in firing properties and action potential measurements across different blades of the dentate gyrus. How do neuronal firing profiles and action potential properties vary across the different sectors of the DG? Are these suprathreshold measurements heterogeneous within each sector? We injected depolarizing current pulses of different amplitudes to assess the firing profile (Fig. 4, *A* and *B*) and several metrics associated with action potentials (Fig. 4, *C* and *D*; Table 3) of DG granule cells. Across the three DG sectors, the firing profile of granule cells (Fig. 4, *B*, Fig. 5, *B–F*) reflected class I excitability,

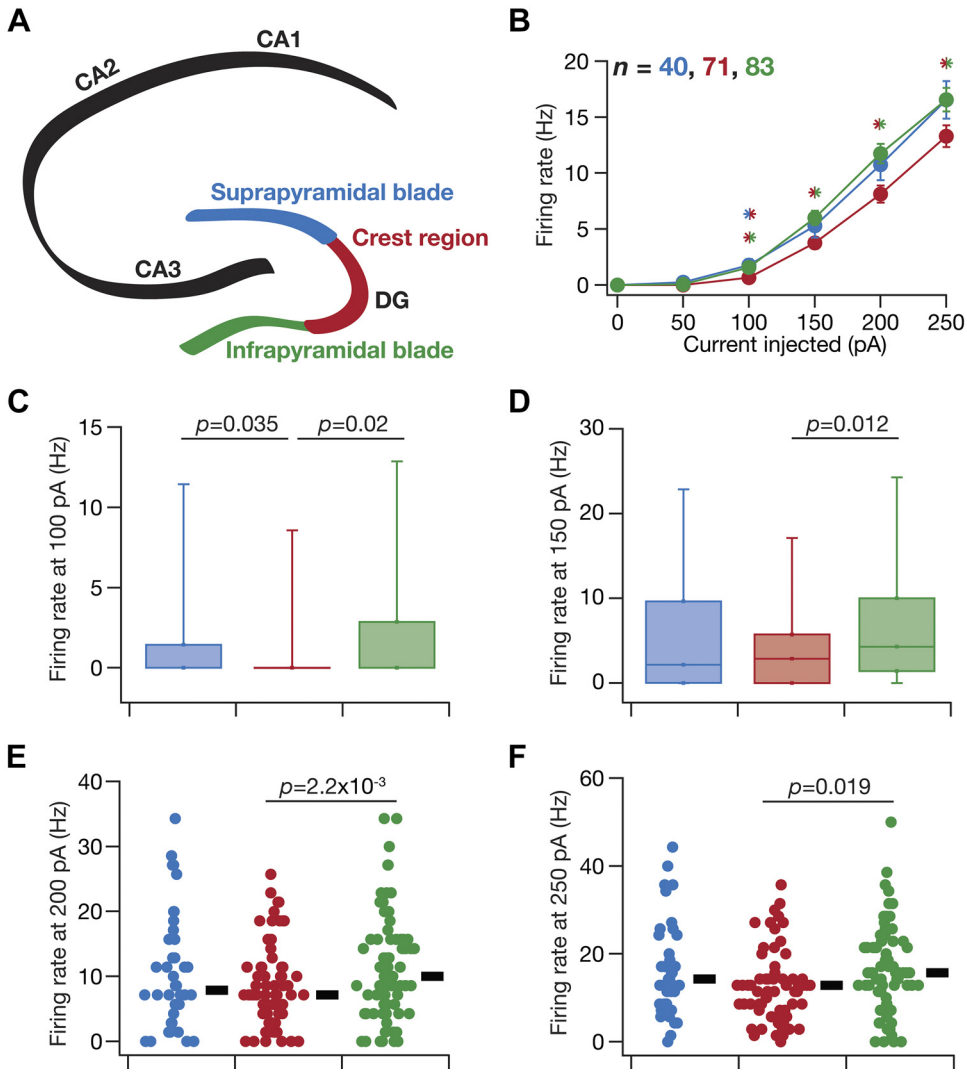

Fig. 5. Heterogeneity in action potential firing frequency of granule cells across the blades of the dentate gyrus (DG). *A*: schematic of the hippocampus proper, showing the different cornu ammonis (CA) subregions (CA1, CA2, and CA3) and the 3 sectors of the DG (infrapyramidal blade, crest region, and suprapyramidal blade). The color codes associated with the 3 DG sectors apply to *B–F*. *B*: frequency of firing plotted as functions of injected current amplitude for the populations of granule cells belonging to the 3 sectors. *$P < 0.05$, Student's *t* test. The 2 colors in the asterisks represent the 2 populations across where significant differences were observed. *C* and *D*: box plots depicting the heterogeneous action potential firing frequency of granule cells from the 3 DG sectors for current injections of amplitude 100 pA (*C*) and 150 pA (*D*). Box plots are employed here because a significant proportion of cells did not fire action potentials, and representation with beeswarm plots exhibited clutters. *E* and *F*: beeswarm plots depicting the heterogeneous action potential firing frequency of granule cells from the 3 DG sectors for current injections of amplitude 200 pA (*E*) and 250 pA (*F*). None of the cells fired spontaneously, and very few cells fired with 50-pA current injection. The black rectangles on *right* of each beeswarm plot represent the median for the specified population. All measurements depicted in this figure were obtained through current injections into a cell resting at resting membrane potential. The *P* values correspond to Wilcoxon rank sum test; *P* values < 0.05 are shown. Neuronal firing rates for each of 100, 150, and 200 pA were significantly different ($P < 0.05$) with both Kruskal–Wallis and ANOVA tests but not those for 50- and 250-pA current injections. Tukey's honestly significant difference test following ANOVA showed significant differences ($P < 0.05$) in firing rates for both 150 and 200 pA between infrapyramidal and crest sectors.

where the neuron was capable of eliciting firing at arbitrarily low frequencies (Hodgkin 1948; Ratté et al. 2013). In addition, beyond rheobase current (which was between 50 and 150 pA in most recorded neurons; Fig. 5, *B–D*), the firing rate increase as a function of injected current was fairly linear (Fig. 5*B*). These observations, along with the low-pass response characteristics and positive temporal summation observed above (Figs. 1–3), pointed to the DG granule neurons acting as integrators of incoming information (Ratté et al. 2013).

We also observed considerable cell-to-cell variability in firing frequencies within each of the three sectors. For instance, for a pulse current injection of 250 pA, the median firing rate of these neurons was ~15 Hz across all three sectors (Fig. 5*F*). However, this rate varied over a large range spanning 0 (no spikes) for certain cells to ~40 Hz in certain others. Thus the mean (Fig. 5*B*) or median (Fig. 5*F*) firing rate values should be treated with caution, because there are cells that do not spike even for 250-pA current injection, whereas certain others spike with rates more than twice the mean/median value. This heterogeneity was observed across all current injections that were assessed (Fig. 5, *C–F*). Importantly, although there was not a large difference in overall range of firing rates observed across the three sectors (Fig. 5, *C–F*), granule cells from the crest region showed significantly ($P < 0.05$, Student's *t* test in Fig. 5*B* and Wilcoxon rank sum test in Fig. 5, *C–F*) reduced excitability

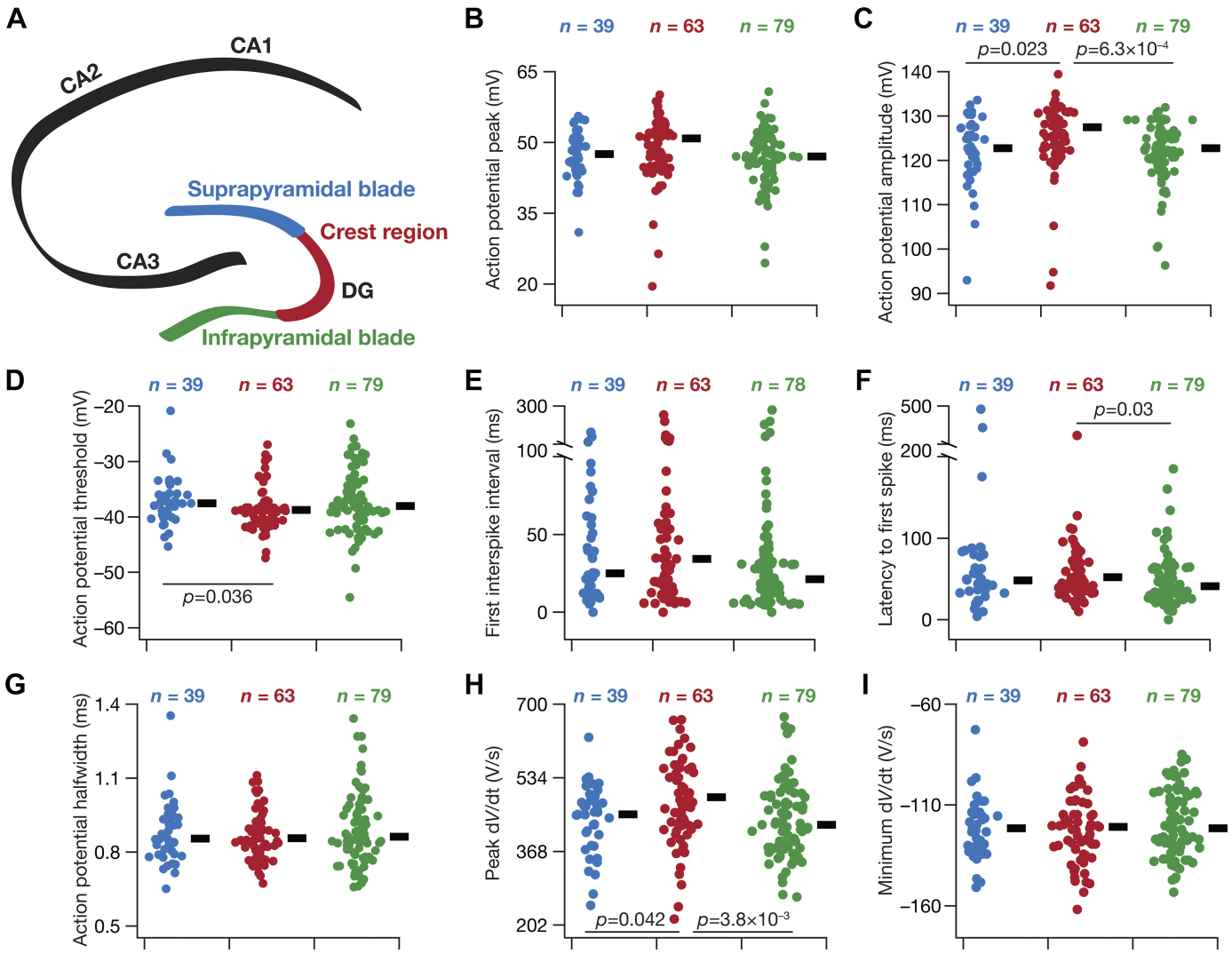

Fig. 6. Heterogeneity in action potential properties of granule cells across the blades of the dentate gyrus (DG). *A*: schematic of the hippocampus proper, showing the different cornu ammonis (CA) subregions (CA1, CA2, and CA3) and the 3 sectors of the DG (infrapyramidal blade, crest region, and suprapyramidal blade). The color codes associated with the 3 DG sectors apply to *B–I*. *B–I*: beeswarm plots depicting the heterogeneous action potential measurements from the 3 DG sectors. The black rectangles on *right* of each beeswarm plot represent the median for the specified population. All measurements depicted in this figure were obtained through current injections into a cell resting at resting membrane potential. The *P* values correspond to Wilcoxon rank sum test; *P* values < 0.05 are shown. All measurements except for action potential amplitude (V_{AP}) and maximum action potential temporal derivative $\left(\left.\frac{dV}{dt}\right|_{AP}^{max}\right)$ were not significantly different ($P > 0.1$) with either Kruskal–Wallis (KW) or ANOVA tests. For V_{AP}, *P* (ANOVA) = 0.03, *P* (KW) = 0.002. For $\left.\frac{dV}{dt}\right|_{AP}^{max}$, *P* (ANOVA) = 0.019, *P* (KW) = 0.01. Tukey's honestly significant difference test following ANOVA yielded significant differences between the infrapyramidal and crest sectors for V_{AP} and $\left.\frac{dV}{dt}\right|_{AP}^{max}$.

compared with cells in the infrapyramidal blade across all measured current injections (Fig. 5, *B–F*).

We next analyzed individual spikes from granule cells recorded from each of the three sectors and derived metrics that quantified spike threshold, width, amplitude, and depolarizing and repolarizing kinetics. Similar to our observations with subthreshold properties (Fig. 2) and action potential firing properties (Fig. 5), we found significant cell-to-cell variability in these measurements even within a given sector (Fig. 6, *B–I*). Across populations, we found action potential amplitude to be significantly lower in granule cells from the crest region compared with those from the two blades (Fig. 6*C*). Action potential threshold was significantly hyperpolarized in crest region cells compared with those in the suprapyramidal blade (Fig. 6*D*). The latency to first spike was significantly lower in the infrapyramidal population of granule cells compared with cells in the crest region (Fig. 6*F*). Finally, the peak derivative of the action potential trace was significantly higher for cells in the crest region compared with cells in the two blades (Fig. 6*H*). We noted that although these differences were statistically significant, the range of values of these measurements from neurons of all three sectors was not very different (Fig. 6, *B–I*). In addition, as the differences in median (Fig. 6) or mean (Table 3) values of these measurements across the sectors were not large (as a fraction of the respective range

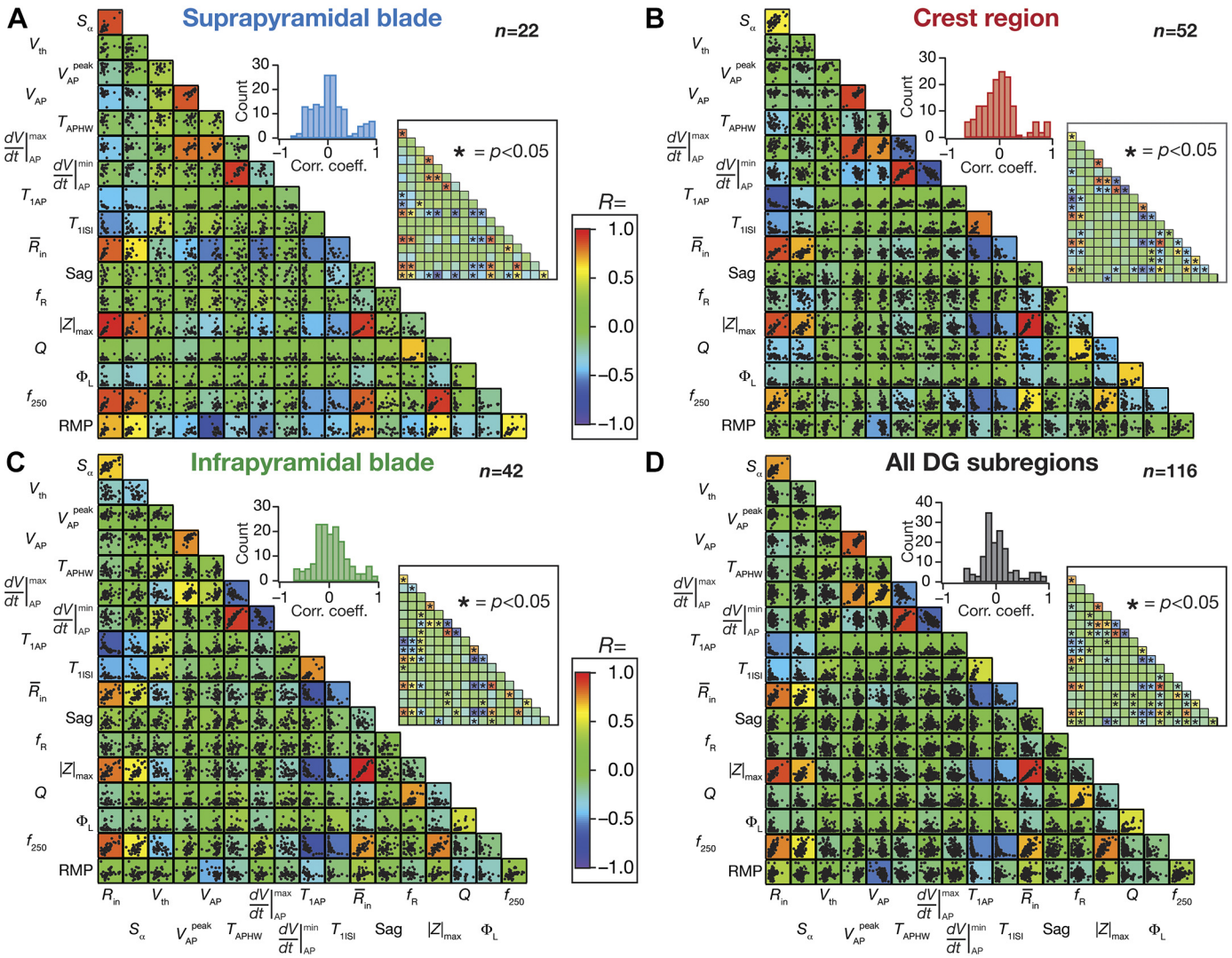

Fig. 7. Differential correlations between sub- and suprathreshold measurements of granule cells across the blades of the dentate gyrus (DG): pairwise scatterplot matrices of 18 sub- and suprathreshold measurements of granule cells recorded from the suprapyramidal blade (*A*), the crest region (*B*), the infrapyramidal blade (*C*), and all these sectors pooled together (*D*). These scatterplot matrices are overlaid on the corresponding color-coded correlation matrices. The *insets* in each panel represent the histograms of the correlation coefficients that are depicted by the correlation matrix and the significance value associated with each scatterplot (the color-coded Pearson's correlation coefficient (R) values are provided as background for asterisks that represent $P < 0.05$). All measurements depicted in this figure were obtained through current injections into a cell resting at resting membrane potential (V_{RMP}). R_{in}, input resistance; S_α, temporal summation ratio; V_{th}, action potential threshold; V_{AP}^{peak}, the maximum voltage value measured on the 1st action potential; V_{AP}, the action potential amplitude, measured as the difference between V_{AP}^{peak} and V_{RMP}; T_{APHW}, full width at half-maximum of the action potential; $\left.\frac{dV}{dt}\right|_{AP}^{max}$ and $\left.\frac{dV}{dt}\right|_{AP}^{min}$, maximum and minimum action potential temporal derivative; T_{1AP}, latency to 1st spike; T_{1ISI}, 1st interspike interval; $\bar{R}_{in}$, input resistance estimate; Sag, sag ratio; f_R, resonance frequency; $|Z|_{max}$, maximum impedance amplitude; Q, resonance strength; Φ_L, total inductive phase; f_{250}, firing rate at 250 pA; RMP, resting membrane potential.

of each measurement), it might be infeasible to infer large differences in action potential properties across DG sectors based on these measurements (especially in light of heterogeneity in each measurement, represented in Fig. 6 and quantified with different measures of degree of heterogeneity in Table 3).

A large proportion of sub- and suprathreshold measurements from all blades of the dentate gyrus exhibited weak pairwise correlations. Are the different sub- and suprathreshold measurements correlated? Are these correlations distinct across the different blades of the DG? Correlations in measurements provide clues about relationships between sub- and suprathreshold measurements, apart from pointing to the possibility of similar ion channel mechanisms underlying these distinct measurements. We plotted pairwise scatterplots of these intrinsic measurements from granule cells recorded from the suprapyramidal blade (Fig. 7*A*), the crest region (Fig. 7*B*), the infrapyramidal blade (Fig. 7*C*), and the pooled population containing cells from all sectors (Fig. 7*D*). We computed Pearson's correlation coefficient for each of these pairwise scatterplots (Fig. 7). Broadly, we found the correlation matrices across the four populations to be fairly similar, with a large number of measurement pairs showing weak pairwise correlations [between −0.4 and +0.4 (Evans 1996); see Fig. 7, *insets*]. A small set of pairs showed strong positive or negative correlations, and this set was also broadly common across the four matrices (Fig. 7). Among measurements that exhibited strong positive correlations were the different measures of excitability (R_{in},

Table 2. *Statistics associated with two subthreshold excitability measurements when respective current stimuli were injected with cell resting at multiple voltages*

Measurement	Voltage	Suprapyramidal Blade	Crest Region	Infrapyramidal Blade
Input resistance estimate, MΩ	−80 mV	89.96 ± 7.69; 32.61; 43.19; 0.36	94.01 ± 5.43; 20.32; 23.25; 0.22	91.51 ± 7.88; 27.29; 22.92; 0.30
	−75 mV	105.10 ± 8.94; 37.91; 48.65; 0.36	113.03 ± 5.76; 21.56; 21.23; 0.19	110.74 ± 8.41; 29.13; 29.32; 0.26
	−70 mV	126.49 ± 10.18; 43.20; 54.88; 0.34	132.65 ± 7.34; 27.47; 34.57; 0.21	127.47 ± 10.44; 36.17; 28.84; 0.28
	−65 mV	150.20 ± 11.35; 48.15; 50.11; 0.32	156.53 ± 8.60; 32.16; 51.35; 0.21	151.38 ± 11.89; 41.19; 57.67; 0.27
	−60 mV	173.70 ± 13.15; 55.80; 60.34; 0.32	178.96 ± 10.85; 40.59; 66.10; 0.23	165.74 ± 10.50; 36.38; 35.41; 0.22
Maximal impedance amplitude, MΩ	−80 mV	128.40 ± 13.31; 56.48; 60.00; 0.44	134.96 ± 8.86; 33.14; 36.98; 0.25	132.99 ± 15.91; 55.12; 43.83; 0.41
	−75 mV	152.09 ± 15.41; 65.39; 73.80; 0.43	161.21 ± 10.41; 38.95; 53.04; 0.24	160.82 ± 16.51; 57.18; 51.17; 0.36
	−70 mV	184.65 ± 18.38; 77.99; 89.50; 0.42	186.07 ± 14.11; 52.78; 80.25; 0.28	185.07 ± 17.78; 61.60; 52.16; 0.33
	−65 mV	215.99 ± 20.62; 87.48; 100.56; 0.41	211.21 ± 16.33; 61.12; 108.90; 0.29	219.42 ± 23.54; 81.54; 64.15; 0.37
	−60 mV	249.89 ± 25.94; 110.03; 101.15; 0.44	241.17 ± 21.84; 81.72; 98.37; 0.34	232.52 ± 18.84; 65.27; 60.19; 0.28

Measurements are means ± SE, and the degree of variability in each measurement is reported as standard deviation, interquartile range, and coefficient of variation. The numbers of cells employed for these analyses were 18, 14, and 12 for the suprapyramidal blade, the crest region, and the infrapyramidal blade, respectively (Fig. 3).

$\overline{R}_{in}$, $|Z|_{max}$, f_{250}) and the measures that were reflective of the depolarizing (V_{AP}, V_{AP}^{peak} and $\left.\frac{dV}{dt}\right|_{AP}^{max}$) or repolarizing ($T_{APHW}$ and $\left.\frac{dV}{dt}\right|_{AP}^{min}$) phase of action potential. Interestingly, temporal summation ratio also showed strong positive correlations with the different measures of excitability. Among measurements that exhibited strong negative correlations were the latency to first spike versus each measure of excitability and the first ISI versus each measure of excitability. Thus, except for a small

Table 3. *Suprathreshold measurements when respective current stimuli were injected with cell resting at V_{RMP}*

Measurement	Symbol	Suprapyramidal Blade	Crest Region	Infrapyramidal Blade
Firing rate at 50 pA, Hz	f_{50}	0.25 ± 0.15 (40); 0.964; 0.00; 3.86	0.00 ± 0.00 (71); 0.00; 0.00; undefined	0.07 ± 0.07 (83); 0.63; 0.00; 9.11
Firing rate at 100 pA, Hz	f_{100}	1.79 ± 0.53 (40); 3.34; 1.43; 1.87	0.66 ± 0.21 (71); 1.80; 0.00; 2.71	1.57 ± 0.31 (83); 2.80; 2.86; 1.79
Firing rate at 150 pA, Hz	f_{150}	5.29 ± 1.05 (40); 6.62; 8.93; 1.25	3.76 ± 0.52 (71); 4.38; 5.71; 1.16	5.99 ± 0.63 (83); 5.70; 8.57; 0.95
Firing rate at 200 pA, Hz	f_{200}	10.75 ± 1.39 (40); 8.82; 10.36; 0.82	8.13 ± 0.76 (71); 6.44; 8.57; 0.79	11.74 ± 0.86 (83); 7.76; 8.57; 0.66
Firing rate at 250 pA, Hz	f_{250}	15.89 ± 1.60 (40); 10.56; 12.5; 0.64	13.30 ± 0.96 (71); 8.13; 8.57; 0.61	16.57 ± 1.06 (83); 9.57; 12.14; 0.58
Action potential threshold, mV	V_{th}	−37.20 ± 0.70 (39); 4.35; 3.91; –0.12	−38.58 ± 0.50 (63); 3.97; 3.2; –0.10	−37.18 ± 0.62 (79); 5.55; 6.54; –0.15
Peak action potential voltage, mV	V_{AP}^{peak}	47.44 ± 0.84 (39); 5.25; 6.49; 0.11	48.14 ± 0.89 (63); 7.04; 7.51; 0.15	46.67 ± 0.68 (79); 6.01; 6.82; 0.13
Action potential amplitude, mV	V_{AP}	122.10 ± 1.27 (39); 7.93; 8.81; 0.06	124.99 ± 1.00 (63); 7.95; 7.86; 0.06	121.86 ± 0.75 (79); 6.71; 6.67; 0.06
Action potential halfwidth, ms	T_{APHW}	0.88 ± 0.02 (39); 0.13; 0.15; 0.14	0.87 ± 0.01 (63); 0.10; 0.13; 0.12	0.89 ± 0.02 (79); 0.15; 0.18; 0.16
Peak dV/dt, V/s	$\left.\frac{dV}{dt}\right\|_{AP}^{max}$	439.13 ± 12.39 (39); 77.35; 92.47; 0.18	476.83 ± 12.02 (63); 95.42; 127.26; 0.2	438.11 ± 9.35 (79); 83.13; 113.22; 0.19
Minimum dV/dt, V/s	$\left.\frac{dV}{dt}\right\|_{AP}^{min}$	−121.25 ± 2.41 (39); 15.03; 17.39; –0.12	−123.94 ± 2.00 (63); 15.89; 19.84; –0.13	−119.05 ± 1.86 (79); 16.54; 25.63; –0.14
Latency to first spike, ms	T_{1AP}	68.94 ± 13.79 (39); 86.1; 45.75; 1.24	58.47 ± 4.70 (63); 37.3; 35.59; 0.64	49.12 ± 3.55 (79); 31.58; 34.54; 0.64
First interspike interval, ms	T_{1ISI}	40.77 ± 6.18 (39); 38.6; 47.05; 0.95	43.10 ± 6.21 (63); 49.29; 39.73; 1.14	35.80 ± 5.57 (78); 49.20; 28.18; 1.37

Measurements are reported as means ± SE (n cells), and the degree of variability in each measurement is reported as standard deviation, interquartile range, and coefficient of variation. V_{RMP}, resting membrane potential.

subset of highly correlated measurements that are derived from common physiological substrates, the large subset of uncorrelated measurements suggest that the set of measurements employed here in characterizing DG granule cells are assessing distinct aspects of their physiology.

Similarity of heterogeneities in granule cell electrophysiological measurements from all blades of the dentate gyrus. What is the degree of heterogeneity in individual physiological measurements? Is the degree of heterogeneity in individual measurements similar across the different sectors of the DG? Do the data spanning the 18 electrophysiological measurements fall into a low-dimensional manifold, with data from the three sectors forming distinct clusters (indicating diverging heterogeneities)? Is the degree of heterogeneity across sectors similar when all measurements are considered together? To address these questions, we first computed three standard quantitative statistical measures of degree of variability (coefficient of variation, interquartile range, and standard deviation) for each of the 22 measurements (Tables 1–3). On the basis of these metrics, we noted that individual measurements had different degrees of variability (smallest for RMP and largest for total inductive phase, based on coefficient of variation) but possessed similar degrees of variability across the three sectors (Tables 1–3). Second, we performed principal component analysis (PCA), a dimensionality reduction technique, on the data set (shown in Fig. 7*D*) comprised of all 18 measurements from the three subregions (Fig. 8). We plotted the data from the three sectors on the axes spanning the three dominant principal components (explaining ~90% of the variance in the data). We found that data from these sectors did not form independent clusters, pointing to similarity in heterogeneities of the data acquired from neurons in the three sectors of the DG (Fig. 8).

DISCUSSION

We performed whole cell patch-clamp electrophysiological recordings of granule cells from the three sectors of the rat DG and systematically measured their sub- and suprathreshold electrophysiological characteristics. Our recordings demonstrate that the granule cells within the three different DG sectors manifest considerable heterogeneities in their intrinsic excitability, temporal summation, action potential characteristics, and frequency-dependent response properties. Assessing neuronal responses to time-varying inputs, we find that DG

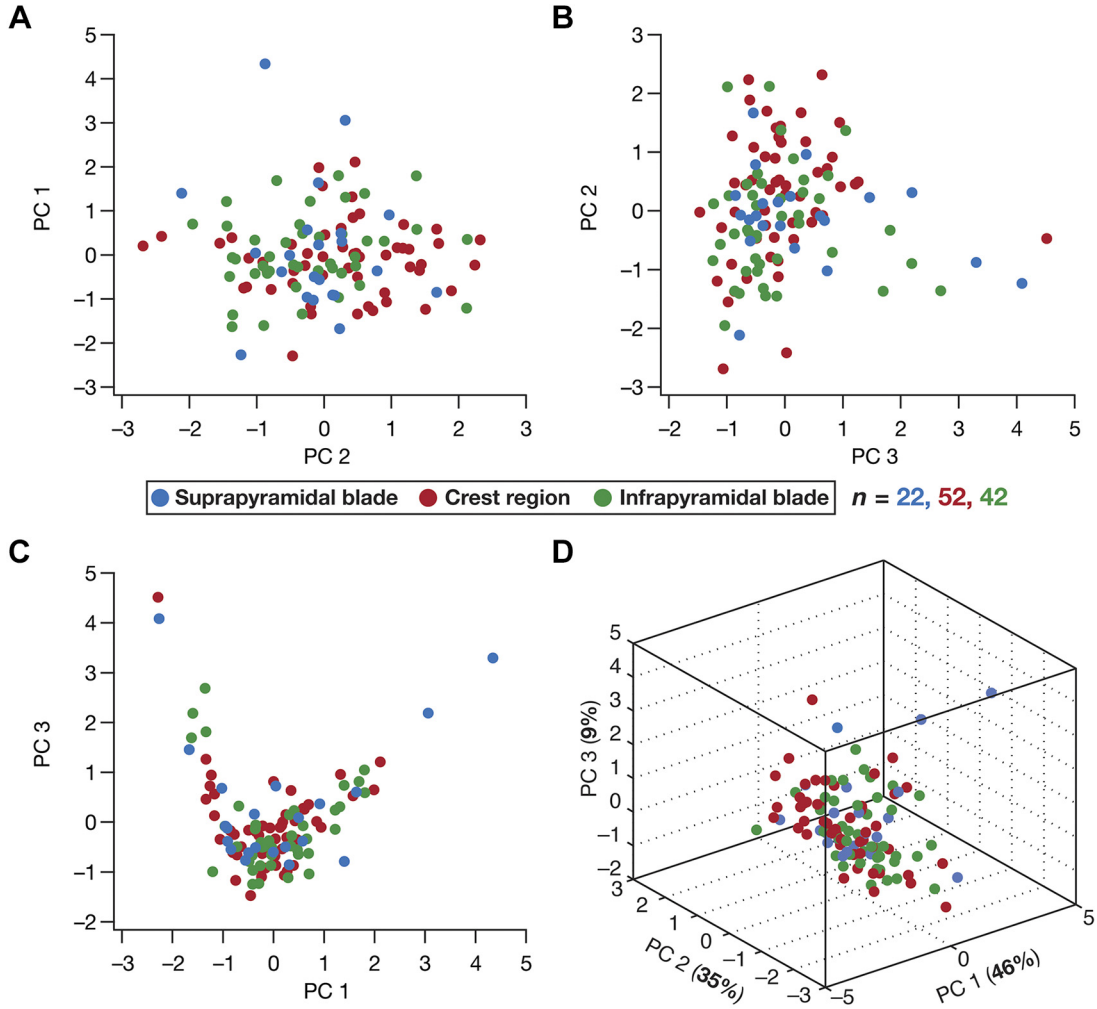

Fig. 8. Principal component analysis (PCA) on the 18-dimensional electrophysiological data unveiled similar heterogeneity across the 3 sectors of the dentate gyrus. *A–C*: pairwise comparison of data with reference to the first 3 principal components (PCs): PC1 vs. PC2 (*A*), PC2 vs. PC3 (*B*), PC3 vs. PC1 (*C*). *D*: 3-dimensional representation of data from the 3 sectors employing the first 3 principal components. The %variance explained by each principal component shown in parentheses in each axis label.

neurons, across all three sectors, showed positive temporal summation of their responses to current injections that mimicked EPSCs. Next, we demonstrated that the impedance amplitude profile manifested low-pass characteristics and the impedance phase profile distinctly lacked positive phase values at all measured frequencies and voltages and for all DG sectors. Consistent with the lack of an inductive component in either the impedance amplitude or phase profiles, neurons across all sectors showed little to no sag in their voltage responses to hyperpolarizing or depolarizing pulse current injections. In what follows, we explore some implications for the expression of heterogeneities inherent to these individual sectors and for the absence of inductive components in the impedance profiles.

Impact of heterogeneities on information processing in the dentate gyrus. The impact of heterogeneities on neural physiology and information processing is well established (Angelo et al. 2012; Anirudhan and Narayanan 2015; Cadwell et al. 2016; Chelaru and Dragoi 2008; Das et al. 2017; Ecker et al. 2011; Fuzik et al. 2016; Gjorgjieva et al. 2016; Goaillard et al. 2009; Grashow et al. 2010; Kohn et al. 2016; Marder 2011; Marder et al. 2014; Marder and Goaillard 2006; Marder and Taylor 2011; Mishra and Narayanan 2019; Mittal and Narayanan 2018; Mukunda and Narayanan 2017; Nusser 2009; Padmanabhan and Urban 2010; Prinz et al. 2004; Rathour and Narayanan 2012a, 2014, 2019; Renart et al. 2003; Shamir and Sompolinsky 2006; Srikanth and Narayanan 2015; Tikidji-Hamburyan et al. 2015; Tripathy et al. 2013; Voliotis et al. 2014; Wang and Buzsáki 1996; Zhou et al. 2013). Within the context of DG physiology, what could be the impact of the heterogeneities observed in their subthreshold (Fig. 2) and suprathreshold (Fig. 5) excitability properties? The DG has been implicated in pattern separation and response decorrelation. There are lines of evidence from different brain regions that heterogeneities in intrinsic neuronal properties could play a critical role in effectuating such response decorrelation (Mishra and Narayanan 2019; Padmanabhan and Urban 2010; Tripathy et al. 2013). The heterogeneities characterized here could contribute to channel and pattern decorrelation in the DG network.

The precise shape of synaptic plasticity profiles in neurons is critically reliant on the local and global excitability properties of the postsynaptic neurons (Anirudhan and Narayanan 2015; Golding et al. 2002; Johnston et al. 2003; Johnston and Narayanan 2008; Narayanan and Johnston 2010; Sehgal et al. 2013; Sjöström and Häusser 2006; Watanabe et al. 2002). This reliance is dependent not only on suprathreshold conductances that enable spike generation and sustain backpropagation of action potentials and dendritic spikes but also on subthreshold conductances that regulate synaptic potentials and their temporal summation (Anirudhan and Narayanan 2015; Chen et al. 2006; Malik and Johnston 2017; Narayanan and Johnston 2010; Nolan et al. 2004). Therefore, the heterogeneities reported here in temporal summation, apart from sub- and suprathreshold excitability properties, could translate to differences in synaptic plasticity profiles of these neurons. Such differential impact of synaptic plasticity protocols, which could concomitantly and differentially alter neuronal intrinsic properties as well (Lopez-Rojas et al. 2016; Stegen et al. 2012; Titley et al. 2017), could also mediate the recruitment of specific cells in memory formation and in the efficacy of memory retrieval (Josselyn and Frankland 2018; Pignatelli et al. 2019; Silva et al. 2009; Yiu et al. 2014; Zhou et al. 2009). Specifically, the baseline differences in excitability reported here could, in conjunction with other mechanisms such as neuromodulation, enable the recruitment of specific cells during memory formation. Together, it is important that experimental interpretations and computational models account for these prominent heterogeneities in the physiological response properties of granule cells.

Granule cells are integrators of afferent information: class I excitability coupled with lack of sag, resonance, and positive impedance phase. Hodgkin (Hodgkin 1948) classified excitability into three distinct classes based on initiation of repetitive action potential firing through constant current injection. Axons that were capable of responding over a wide range of frequencies, especially at arbitrarily low frequencies, were designated as class I. Axons that were classified as class II exhibited a pronounced supernormal phase, whereby the frequency of action potential firing was largely invariant to the injected current amplitude after the first spike was elicited (for currents beyond the rheobase current). Class III axons were those that elicited a second spike (beyond the first spike) only with difficulty or not at all (Hodgkin 1948). This classification has provided an invaluable tool to understand neuronal excitability, neural coding spike initiation dynamics, neuronal operating characteristics and phase resetting curves in a broadly unified manner, with the ionic mechanisms underlying these classes of excitability well understood (Das et al. 2017; Das and Narayanan 2014, 2015, 2017; Ermentrout 1996; Hodgkin 1948; Prescott et al. 2006, 2008a, 2008b; Ratté et al. 2013). Specifically, it is now recognized that the different classes of excitability are consequent to cooperation or competition between fast inward currents and slow outward currents. Cooperation between these two classes of currents yields class I excitability, whereas competition yields class II/III excitability. Importantly, these classes of excitability have been linked to the ability of neurons to act as integrators (class I) or as coincidence detectors (class II/III), with the synergistic interactions among channels capable of sliding the operating mode of a neuron along the integrator–coincidence detector continuum (Das et al. 2017; Das and Narayanan 2014, 2015, 2017; Ratté et al. 2013).

Our *f–I* curve results demonstrate that the DG granule cells are capable of firing at arbitrarily low frequencies, with firing frequency clearly dependent on input current injection (Fig. 5*B*), pointing to class I excitability characteristics. In addition, the absence of sag, resonance, and positive impedance phase also point to absence of a dominant slow outward current that can contribute to class II/III excitability or coincidence detection capabilities (Das et al. 2017; Das and Narayanan 2014, 2015, 2017; Krueppel et al. 2011; Ratté et al. 2013). Together these results clearly point to dentate granule cell somata acting as integrators of afferent information (also see Aimone et al. 2011). However, it should be noted that operating modes of neurons could change in response to several factors, including activity-dependent plasticity of channels and receptors, neuromodulation, and changes in afferent activity patterns (Das et al. 2017; Das and Narayanan 2014, 2015, 2017; Prescott et al. 2006, 2008a, 2008b; Ratté et al. 2013). Future studies should therefore assess the spike-triggered average of DG neurons to understand their operating modes, the roles of different ion

channels in regulating operating mode across their somato-dendritic axis, and the information processing strategies employed by the DG neurons (Das et al. 2017; Das and Narayanan 2014, 2015, 2017; Krueppel et al. 2011; Schmidt-Hieber et al. 2007).

Despite the well-established expression of the hyperpolarization-activated cyclic nucleotide-gated (HCN) channels in granule cells (Bender et al. 2003; Krueppel et al. 2011; Stegen et al. 2012; Surges et al. 2012), they do not express impedance resonance or positive impedance phase (Figs. 1–3), unlike CA1 pyramidal neurons or entorhinal stellate neurons (Das et al. 2017; Erchova et al. 2004; Hu et al. 2002, 2009; Mittal and Narayanan 2018; Narayanan and Johnston 2007, 2008). Consistent with this, these neurons do not exhibit a strong voltage sag in the response to pulse currents (Fig. 1*A*, Fig. 2*E*, Fig. 3*B*), a time-domain equivalent of resonance expression in the frequency domain (Hutcheon and Yarom 2000). However, it is established that the expression of impedance resonance (and voltage sag) is dependent not just on the expression of a resonating conductance but on the density of the resonating conductance and the leak conductance in the neuron (Hutcheon et al. 1996a, 1996b; Hutcheon and Yarom 2000; Narayanan and Johnston 2007, 2008; Rathour et al. 2016; Rathour and Narayanan 2012a, 2012b, 2014; Zemankovics et al. 2010), on the time constants of the resonating conductance (Hutcheon et al. 1996a; Hutcheon and Yarom 2000; Narayanan and Johnston 2008; Rathour and Narayanan 2012a), on morphological properties (Dhupia et al. 2015), on the relative expression profiles of other subthreshold channels and interactions of these channels with the resonating conductances (Das et al. 2017; Rathour et al. 2016; Rathour and Narayanan 2012a, 2014, 2019; Stegen et al. 2012). One potential reason for the absence of the voltage sag/resonance in DG granule cells could be the established inverse relationship between the activation time constant of the resonating conductance and resonance frequency/voltage sag (Hutcheon et al. 1996a; Hutcheon and Yarom 2000; Narayanan and Johnston 2008; Rathour and Narayanan 2012a). HCN channels in DG granule cells are endowed with extremely slow kinetics (Surges et al. 2012), with the activation time constant in the ~500 ms range [compared with ~50 ms in CA1 pyramidal neurons (Magee 1998)]. The frequency-dependent response analyses presented in our study also provide indirect evidence for the expression of HCN channels, through the reduction of excitability at hyperpolarized voltages (Fig. 3), through a hyperpolarization-induced suppression of gain that is dominant at low frequencies (Fig. 1*E*), and through the reduction in the capacitive lag in the impedance profiles (Fig. 1*F*) with hyperpolarization.

Future directions. Future studies should explore all of the somato-dendritic, infrapyramidal-suprapyramidal, dorso-ventral, and superficial-deep axes of the DG and characterize intrinsic heterogeneities expressed not just in granule cells but also in other cell types including the basket cells, the mossy cells, and the semilunar granule cells (Amaral et al. 2007; Williams et al. 2007). In addition, these studies should explore whether there are systematic gradients in voltage-gated and ligand-gated channels across these different axes, which would alter the processing and encoding strategies associated with these neurons. The assessment of these heterogeneities and gradients is especially essential, given the gradients that are observed in intrinsic and synaptic properties of other spatially proximal cell types, including the CA1 pyramidal neurons and entorhinal stellate cells (Cembrowski et al. 2016; Cembrowski and Spruston 2019; Danielson et al. 2016; Dougherty et al. 2012, 2013; Giocomo et al. 2007; Giocomo and Hasselmo 2009; Kjelstrup et al. 2008; Lee et al. 2014; Malik et al. 2016; Marcelin et al. 2012; Maroso et al. 2016; Mizuseki et al. 2011; Soltesz and Losonczy 2018; Strange et al. 2014; Valero et al. 2015). Finally, the data set presented in this study was obtained in the presence of intact synaptic activity. Given the potential impact of tonic and background synaptic activity (Chance et al. 2002; Destexhe et al. 2003), future studies could quantify the heterogeneities across these sectors in the presence of synaptic blockers. Together, our analyses emphasize that experimental interpretations and computational models should not extrapolate DG cell excitability from summary statistics or treat DG neurons as a homogeneous population but should account for the extensive heterogeneities prevalent in the physiological response properties of granule cells.

ACKNOWLEDGMENTS

The authors thank Divyansh Mittal for helpful discussions and for comments on a draft of this manuscript.

GRANTS

This work was supported by the Wellcome Trust-Department of Biotechnology (DBT) India Alliance (Senior Fellowship to R. Narayanan; IA/S/16/2/502727), the DBT through the DBT-Indian Institute of Science (IISc) partnership program (R. Narayanan), the Revati and Satya Nadham Atluri Chair at IISc (R. Narayanan), and the Ministry of Human Resource Development (R. Narayanan and P. Mishra).

DISCLOSURES

No conflicts of interest, financial or otherwise, are declared by the authors.

AUTHOR CONTRIBUTIONS

P.M. and R.N. conceived and designed research; P.M. performed experiments; P.M. and R.N. analyzed data; P.M. and R.N. interpreted results of experiments; P.M. and R.N. prepared figures; P.M. and R.N. drafted manuscript; P.M. and R.N. edited and revised manuscript; P.M. and R.N. approved final version of manuscript.

REFERENCES

Aimone JB, Deng W, Gage FH. Resolving new memories: a critical look at the dentate gyrus, adult neurogenesis, and pattern separation. *Neuron* 70: 589–596, 2011. doi:10.1016/j.neuron.2011.05.010.

Aimone JB, Li Y, Lee SW, Clemenson GD, Deng W, Gage FH. Regulation and function of adult neurogenesis: from genes to cognition. *Physiol Rev* 94: 991–1026, 2014. doi:10.1152/physrev.00004.2014.

Amaral DG, Scharfman HE, Lavenex P. The dentate gyrus: fundamental neuroanatomical organization (dentate gyrus for dummies). *Prog Brain Res* 163: 3–22, 2007. doi:10.1016/S0079-6123(07)63001-5.

Andersen P, Morris R, Amaral D, Bliss T, O'Keefe J (Editors). *The Hippocampus Book***.** New York: Oxford Univ. Press, 2006.

Angelo K, Rancz EA, Pimentel D, Hundahl C, Hannibal J, Fleischmann A, Pichler B, Margrie TW. A biophysical signature of network affiliation and sensory processing in mitral cells. *Nature* 488: 375–378, 2012. doi:10.1038/nature11291.

Anirudhan A, Narayanan R. Analogous synaptic plasticity profiles emerge from disparate channel combinations. *J Neurosci* 35: 4691–4705, 2015. doi:10.1523/JNEUROSCI.4223-14.2015.

Ashhad S, Johnston D, Narayanan R. Activation of $InsP_3$ receptors is sufficient for inducing graded intrinsic plasticity in rat hippocampal pyramidal neurons. *J Neurophysiol* 113: 2002–2013, 2015. doi:10.1152/jn.00833.2014.

Ashhad S, Narayanan R. Active dendrites regulate the impact of gliotransmission on rat hippocampal pyramidal neurons. *Proc Natl Acad Sci USA* 113: E3280–E3289, 2016. doi:10.1073/pnas.1522180113.

Bakker A, Kirwan CB, Miller M, Stark CE. Pattern separation in the human hippocampal CA3 and dentate gyrus. *Science* 319: 1640–1642, 2008. doi:10.1126/science.1152882.

Bender RA, Soleymani SV, Brewster AL, Nguyen ST, Beck H, Mathern GW, Baram TZ. Enhanced expression of a specific hyperpolarization-activated cyclic nucleotide-gated cation channel (HCN) in surviving dentate gyrus granule cells of human and experimental epileptic hippocampus. *J Neurosci* 23: 6826–6836, 2003. doi:10.1523/JNEUROSCI.23-17-06826.2003.

Bland BH. The physiology and pharmacology of hippocampal formation theta rhythms. *Prog Neurobiol* 26: 1–54, 1986. doi:10.1016/0301-0082(86)90019-5.

Bliss TV, Lomo T. Long-lasting potentiation of synaptic transmission in the dentate area of the anaesthetized rabbit following stimulation of the perforant path. *J Physiol* 232: 331–356, 1973. doi:10.1113/jphysiol.1973.sp010273.

Buzsáki G. Theta oscillations in the hippocampus. *Neuron* 33: 325–340, 2002. doi:10.1016/S0896-6273(02)00586-X.

Cadwell CR, Palasantza A, Jiang X, Berens P, Deng Q, Yilmaz M, Reimer J, Shen S, Bethge M, Tolias KF, Sandberg R, Tolias AS. Electrophysiological, transcriptomic and morphologic profiling of single neurons using Patch-seq. *Nat Biotechnol* 34: 199–203, 2016. doi:10.1038/nbt.3445.

Cembrowski MS, Bachman JL, Wang L, Sugino K, Shields BC, Spruston N. Spatial gene-expression gradients underlie prominent heterogeneity of CA1 pyramidal neurons. *Neuron* 89: 351–368, 2016. doi:10.1016/j.neuron.2015.12.013.

Cembrowski MS, Spruston N. Heterogeneity within classical cell types is the rule: lessons from hippocampal pyramidal neurons. *Nat Rev Neurosci* 20: 193–204, 2019. doi:10.1038/s41583-019-0125-5.

Chance FS, Abbott LF, Reyes AD. Gain modulation from background synaptic input. *Neuron* 35: 773–782, 2002. doi:10.1016/S0896-6273(02)00820-6.

Chawla MK, Guzowski JF, Ramirez-Amaya V, Lipa P, Hoffman KL, Marriott LK, Worley PF, McNaughton BL, Barnes CA. Sparse, environmentally selective expression of Arc RNA in the upper blade of the rodent fascia dentata by brief spatial experience. *Hippocampus* 15: 579–586, 2005. doi:10.1002/hipo.20091.

Chelaru MI, Dragoi V. Efficient coding in heterogeneous neuronal populations. *Proc Natl Acad Sci USA* 105: 16344–16349, 2008. doi:10.1073/pnas.0807744105.

Chen X, Yuan LL, Zhao C, Birnbaum SG, Frick A, Jung WE, Schwarz TL, Sweatt JD, Johnston D. Deletion of Kv4.2 gene eliminates dendritic A-type K^+ current and enhances induction of long-term potentiation in hippocampal CA1 pyramidal neurons. *J Neurosci* 26: 12143–12151, 2006. doi:10.1523/JNEUROSCI.2667-06.2006.

Claiborne BJ, Amaral DG, Cowan WM. A light and electron microscopic analysis of the mossy fibers of the rat dentate gyrus. *J Comp Neurol* 246: 435–458, 1986. doi:10.1002/cne.902460403.

Claiborne BJ, Amaral DG, Cowan WM. Quantitative, three-dimensional analysis of granule cell dendrites in the rat dentate gyrus. *J Comp Neurol* 302: 206–219, 1990. doi:10.1002/cne.903020203.

Cole KS. Rectification and inductance in the squid giant axon. *J Gen Physiol* 25: 29–51, 1941. doi:10.1085/jgp.25.1.29.

Cole KS, Baker RF. Longitudinal impedance of the squid giant axon. *J Gen Physiol* 24: 771–788, 1941a. doi:10.1085/jgp.24.6.771.

Cole KS, Baker RF. Transverse impedance of the squid giant axon during current flow. *J Gen Physiol* 24: 535–549, 1941b. doi:10.1085/jgp.24.4.535.

Colgin LL. Mechanisms and functions of theta rhythms. *Annu Rev Neurosci* 36: 295–312, 2013. doi:10.1146/annurev-neuro-062012-170330.

Colgin LL. Rhythms of the hippocampal network. *Nat Rev Neurosci* 17: 239–249, 2016. doi:10.1038/nrn.2016.21.

Danielson NB, Turi GF, Ladow M, Chavlis S, Petrantonakis PC, Poirazi P, Losonczy A. In vivo imaging of dentate gyrus mossy cells in behaving mice. *Neuron* 93: 552–559.e554, 2017. doi:10.1016/j.neuron.2016.12.019.

Danielson NB, Zaremba JD, Kaifosh P, Bowler J, Ladow M, Losonczy A. Sublayer-specific coding dynamics during spatial navigation and learning in hippocampal area CA1. *Neuron* 91: 652–665, 2016. doi:10.1016/j.neuron.2016.06.020.

Das A, Narayanan R. Active dendrites regulate spectral selectivity in location-dependent spike initiation dynamics of hippocampal model neurons. *J Neurosci* 34: 1195–1211, 2014. doi:10.1523/JNEUROSCI.3203-13.2014.

Das A, Narayanan R. Active dendrites mediate stratified gamma-range coincidence detection in hippocampal model neurons. *J Physiol* 593: 3549–3576, 2015. doi:10.1113/JP270688.

Das A, Narayanan R. Theta-frequency selectivity in the somatic spike-triggered average of rat hippocampal pyramidal neurons is dependent on HCN channels. *J Neurophysiol* 118: 2251–2266, 2017. doi:10.1152/jn.00356.2017.

Das A, Rathour RK, Narayanan R. Strings on a violin: location dependence of frequency tuning in active dendrites. *Front Cell Neurosci* 11: 72, 2017. doi:10.3389/fncel.2017.00072.

Desmond NL, Levy WB. A quantitative anatomical study of the granule cell dendritic fields of the rat dentate gyrus using a novel probabilistic method. *J Comp Neurol* 212: 131–145, 1982. doi:10.1002/cne.902120204.

Desmond NL, Levy WB. Granule cell dendritic spine density in the rat hippocampus varies with spine shape and location. *Neurosci Lett* 54: 219–224, 1985. doi:10.1016/S0304-3940(85)80082-3.

Destexhe A, Rudolph M, Paré D. The high-conductance state of neocortical neurons in vivo. *Nat Rev Neurosci* 4: 739–751, 2003. [Erratum in *Nat Rev Neurosci* 4: 1019, 2003.] doi:10.1038/nrn1198.

Dhupia N, Rathour RK, Narayanan R. Dendritic atrophy constricts functional maps in resonance and impedance properties of hippocampal model neurons. *Front Cell Neurosci* 8: 456, 2015. doi:10.3389/fncel.2014.00456.

Diamantaki M, Frey M, Berens P, Preston-Ferrer P, Burgalossi A. Sparse activity of identified dentate granule cells during spatial exploration. *eLife* 5: e20252, 2016. doi:10.7554/eLife.20252.

Dougherty KA, Islam T, Johnston D. Intrinsic excitability of CA1 pyramidal neurones from the rat dorsal and ventral hippocampus. *J Physiol* 590: 5707–5722, 2012. doi:10.1113/jphysiol.2012.242693.

Dougherty KA, Nicholson DA, Diaz L, Buss EW, Neuman KM, Chetkovich DM, Johnston D. Differential expression of HCN subunits alters voltage-dependent gating of h-channels in CA1 pyramidal neurons from dorsal and ventral hippocampus. *J Neurophysiol* 109: 1940–1953, 2013. doi:10.1152/jn.00010.2013.

Ecker AS, Berens P, Tolias AS, Bethge M. The effect of noise correlations in populations of diversely tuned neurons. *J Neurosci* 31: 14272–14283, 2011. doi:10.1523/JNEUROSCI.2539-11.2011.

Erchova I, Kreck G, Heinemann U, Herz AV. Dynamics of rat entorhinal cortex layer II and III cells: characteristics of membrane potential resonance at rest predict oscillation properties near threshold. *J Physiol* 560: 89–110, 2004. doi:10.1113/jphysiol.2004.069930.

Ermentrout B. Type I membranes, phase resetting curves, and synchrony. *Neural Comput* 8: 979–1001, 1996. doi:10.1162/neco.1996.8.5.979.

Evans JD. *Straightforward Statistics for the Behavioral Sciences*. Boston, MA: Brooks/Cole, 1996.

Fricke RA, Prince DA. Electrophysiology of dentate gyrus granule cells. *J Neurophysiol* 51: 195–209, 1984. doi:10.1152/jn.1984.51.2.195.

Fuzik J, Zeisel A, Máté Z, Calvigioni D, Yanagawa Y, Szabó G, Linnarsson S, Harkany T. Integration of electrophysiological recordings with single-cell RNA-seq data identifies neuronal subtypes. *Nat Biotechnol* 34: 175–183, 2016. doi:10.1038/nbt.3443.

Gallitano AL, Satvat E, Gil M, Marrone DF. Distinct dendritic morphology across the blades of the rodent dentate gyrus. *Synapse* 70: 277–282, 2016. doi:10.1002/syn.21900.

Gimbarzevsky B, Miura RM, Puil E. Impedance profiles of peripheral and central neurons. *Can J Physiol Pharmacol* 62: 460–462, 1984. doi:10.1139/y84-074.

Giocomo LM, Hasselmo ME. Knock-out of HCN1 subunit flattens dorsal-ventral frequency gradient of medial entorhinal neurons in adult mice. *J Neurosci* 29: 7625–7630, 2009. doi:10.1523/JNEUROSCI.0609-09.2009.

Giocomo LM, Zilli EA, Fransén E, Hasselmo ME. Temporal frequency of subthreshold oscillations scales with entorhinal grid cell field spacing. *Science* 315: 1719–1722, 2007. doi:10.1126/science.1139207.

Gjorgjieva J, Drion G, Marder E. Computational implications of biophysical diversity and multiple timescales in neurons and synapses for circuit performance. *Curr Opin Neurobiol* 37: 44–52, 2016. doi:10.1016/j.conb.2015.12.008.

Goaillard JM, Taylor AL, Schulz DJ, Marder E. Functional consequences of animal-to-animal variation in circuit parameters. *Nat Neurosci* 12: 1424–1430, 2009. doi:10.1038/nn.2404.

Golding NL, Staff NP, Spruston N. Dendritic spikes as a mechanism for cooperative long-term potentiation. *Nature* 418: 326–331, 2002. doi:10.1038/nature00854.

GoodSmith D, Chen X, Wang C, Kim SH, Song H, Burgalossi A, Christian KM, Knierim JJ. Spatial representations of granule cells and mossy cells of the dentate gyrus. *Neuron* 93: 677–690.e5, 2017. doi:10.1016/j.neuron.2016.12.026.

Grashow R, Brookings T, Marder E. Compensation for variable intrinsic neuronal excitability by circuit-synaptic interactions. *J Neurosci* 30: 9145–9156, 2010. doi:10.1523/JNEUROSCI.0980-10.2010.

Green EJ, Juraska JM. The dendritic morphology of hippocampal dentate granule cells varies with their position in the granule cell layer: a quantitative Golgi study. *Exp Brain Res* 59: 582–586, 1985. doi:10.1007/BF00261350.

Heigele S, Sultan S, Toni N, Bischofberger J. Bidirectional GABAergic control of action potential firing in newborn hippocampal granule cells. *Nat Neurosci* 19: 263–270, 2016. doi:10.1038/nn.4218.

Hodgkin AL. The local electric changes associated with repetitive action in a non-medullated axon. *J Physiol* 107: 165–181, 1948. doi:10.1113/jphysiol.1948.sp004260.

Hu H, Vervaeke K, Graham LJ, Storm JF. Complementary theta resonance filtering by two spatially segregated mechanisms in CA1 hippocampal pyramidal neurons. *J Neurosci* 29: 14472–14483, 2009. doi:10.1523/JNEUROSCI.0187-09.2009.

Hu H, Vervaeke K, Storm JF. Two forms of electrical resonance at theta frequencies, generated by M-current, h-current and persistent Na^+ current in rat hippocampal pyramidal cells. *J Physiol* 545: 783–805, 2002. doi:10.1113/jphysiol.2002.029249.

Hutcheon B, Miura RM, Puil E. Models of subthreshold membrane resonance in neocortical neurons. *J Neurophysiol* 76: 698–714, 1996a. doi:10.1152/jn.1996.76.2.698.

Hutcheon B, Miura RM, Puil E. Subthreshold membrane resonance in neocortical neurons. *J Neurophysiol* 76: 683–697, 1996b. doi:10.1152/jn.1996.76.2.683.

Hutcheon B, Yarom Y. Resonance, oscillation and the intrinsic frequency preferences of neurons. *Trends Neurosci* 23: 216–222, 2000. doi:10.1016/S0166-2236(00)01547-2.

Johnston D, Christie BR, Frick A, Gray R, Hoffman DA, Schexnayder LK, Watanabe S, Yuan LL. Active dendrites, potassium channels and synaptic plasticity. *Philos Trans R Soc Lond B Biol Sci* 358: 667–674, 2003. doi:10.1098/rstb.2002.1248.

Johnston D, Narayanan R. Active dendrites: colorful wings of the mysterious butterflies. *Trends Neurosci* 31: 309–316, 2008. doi:10.1016/j.tins.2008.03.004.

Josselyn SA, Frankland PW. Memory allocation: mechanisms and function. *Annu Rev Neurosci* 41: 389–413, 2018. doi:10.1146/annurev-neuro-080317-061956.

Kjelstrup KB, Solstad T, Brun VH, Hafting T, Leutgeb S, Witter MP, Moser EI, Moser MB. Finite scale of spatial representation in the hippocampus. *Science* 321: 140–143, 2008. doi:10.1126/science.1157086.

Kohn A, Coen-Cagli R, Kanitscheider I, Pouget A. Correlations and neuronal population information. *Annu Rev Neurosci* 39: 237–256, 2016. doi:10.1146/annurev-neuro-070815-013851.

Kropff E, Yang SM, Schinder AF. Dynamic role of adult-born dentate granule cells in memory processing. *Curr Opin Neurobiol* 35: 21–26, 2015. doi:10.1016/j.conb.2015.06.002.

Krueppel R, Remy S, Beck H. Dendritic integration in hippocampal dentate granule cells. *Neuron* 71: 512–528, 2011. doi:10.1016/j.neuron.2011.05.043.

Lee SH, Marchionni I, Bezaire M, Varga C, Danielson N, Lovett-Barron M, Losonczy A, Soltesz I. Parvalbumin-positive basket cells differentiate among hippocampal pyramidal cells. *Neuron* 82: 1129–1144, 2014. doi:10.1016/j.neuron.2014.03.034.

Leutgeb JK, Leutgeb S, Moser MB, Moser EI. Pattern separation in the dentate gyrus and CA3 of the hippocampus. *Science* 315: 961–966, 2007. doi:10.1126/science.1135801.

Li L, Sultan S, Heigele S, Schmidt-Salzmann C, Toni N, Bischofberger J. Silent synapses generate sparse and orthogonal action potential firing in adult-born hippocampal granule cells. *eLife* 6: e23612, 2017. doi:10.7554/eLife.23612.

Liu YB, Lio PA, Pasternak JF, Trommer BL. Developmental changes in membrane properties and postsynaptic currents of granule cells in rat dentate gyrus. *J Neurophysiol* 76: 1074–1088, 1996. doi:10.1152/jn.1996.76.2.1074.

Lopez-Rojas J, Heine M, Kreutz MR. Plasticity of intrinsic excitability in mature granule cells of the dentate gyrus. *Sci Rep* 6: 21615, 2016. doi:10.1038/srep21615.

Magee JC. Dendritic hyperpolarization-activated currents modify the integrative properties of hippocampal CA1 pyramidal neurons. *J Neurosci* 18: 7613–7624, 1998. doi:10.1523/JNEUROSCI.18-19-07613.1998.

Magee JC. Dendritic I_h normalizes temporal summation in hippocampal CA1 neurons. *Nat Neurosci* 2: 508–514, 1999. [Erratum in *Nat Neurosci* 2: 848, 1999.] doi:10.1038/9158.

Malik R, Dougherty KA, Parikh K, Byrne C, Johnston D. Mapping the electrophysiological and morphological properties of CA1 pyramidal neurons along the longitudinal hippocampal axis. *Hippocampus* 26: 341–361, 2016. doi:10.1002/hipo.22526.

Malik R, Johnston D. Dendritic GIRK channels gate the integration window, plateau potentials, and induction of synaptic plasticity in dorsal but not ventral CA1 neurons. *J Neurosci* 37: 3940–3955, 2017. doi:10.1523/JNEUROSCI.2784-16.2017.

Marcelin B, Liu Z, Chen Y, Lewis AS, Becker A, McClelland S, Chetkovich DM, Migliore M, Baram TZ, Esclapez M, Bernard C. Dorsoventral differences in intrinsic properties in developing CA1 pyramidal cells. *J Neurosci* 32: 3736–3747, 2012. doi:10.1523/JNEUROSCI.5870-11.2012.

Marder E. Variability, compensation, and modulation in neurons and circuits. *Proc Natl Acad Sci USA* 108, *Suppl* 3: 15542–15548, 2011. doi:10.1073/pnas.1010674108.

Marder E, Goaillard JM. Variability, compensation and homeostasis in neuron and network function. *Nat Rev Neurosci* 7: 563–574, 2006. doi:10.1038/nrn1949.

Marder E, O'Leary T, Shruti S. Neuromodulation of circuits with variable parameters: single neurons and small circuits reveal principles of state-dependent and robust neuromodulation. *Annu Rev Neurosci* 37: 329–346, 2014. doi:10.1146/annurev-neuro-071013-013958.

Marder E, Taylor AL. Multiple models to capture the variability in biological neurons and networks. *Nat Neurosci* 14: 133–138, 2011. doi:10.1038/nn.2735.

Maroso M, Szabo GG, Kim HK, Alexander A, Bui AD, Lee SH, Lutz B, Soltesz I. Cannabinoid control of learning and memory through HCN channels. *Neuron* 89: 1059–1073, 2016. doi:10.1016/j.neuron.2016.01.023.

Marrone DF, Ramirez-Amaya V, Barnes CA. Neurons generated in senescence maintain capacity for functional integration. *Hippocampus* 22: 1134–1142, 2012a. doi:10.1002/hipo.20959.

Marrone DF, Satvat E, Shaner MJ, Worley PF, Barnes CA. Attenuated long-term Arc expression in the aged fascia dentata. *Neurobiol Aging* 33: 979–990, 2012b. doi:10.1016/j.neurobiolaging.2010.07.022.

Mauro A. Anomalous impedance, a phenomenological property of time-variant resistance. An analytic review. *Biophys J* 1: 353–372, 1961. doi:10.1016/S0006-3495(61)86894-X.

Mauro A, Conti F, Dodge F, Schor R. Subthreshold behavior and phenomenological impedance of the squid giant axon. *J Gen Physiol* 55: 497–523, 1970. doi:10.1085/jgp.55.4.497.

McHugh TJ, Jones MW, Quinn JJ, Balthasar N, Coppari R, Elmquist JK, Lowell BB, Fanselow MS, Wilson MA, Tonegawa S. Dentate gyrus NMDA receptors mediate rapid pattern separation in the hippocampal network. *Science* 317: 94–99, 2007. doi:10.1126/science.1140263.

Mishra P, Narayanan R. Disparate forms of heterogeneities and interactions among them drive channel decorrelation in the dentate gyrus: degeneracy and dominance. *Hippocampus* 29: 378–403, 2019. doi:10.1002/hipo.23035.

Mittal D, Narayanan R. Degeneracy in the robust expression of spectral selectivity, subthreshold oscillations, and intrinsic excitability of entorhinal stellate cells. *J Neurophysiol* 120: 576–600, 2018. doi:10.1152/jn.00136.2018.

Mizuseki K, Diba K, Pastalkova E, Buzsáki G. Hippocampal CA1 pyramidal cells form functionally distinct sublayers. *Nat Neurosci* 14: 1174–1181, 2011. doi:10.1038/nn.2894.

Mody I, Köhr G, Otis TS, Staley KJ. The electrophysiology of dentate gyrus granule cells in whole-cell recordings. *Epilepsy Res Suppl* 7: 159–168, 1992.

Mukunda CL, Narayanan R. Degeneracy in the regulation of short-term plasticity and synaptic filtering by presynaptic mechanisms. *J Physiol* 595: 2611–2637, 2017. doi:10.1113/JP273482.

Narayanan R, Dougherty KJ, Johnston D. Calcium store depletion induces persistent perisomatic increases in the functional density of h channels in hippocampal pyramidal neurons. *Neuron* 68: 921–935, 2010. doi:10.1016/j.neuron.2010.11.033.

Narayanan R, Johnston D. Long-term potentiation in rat hippocampal neurons is accompanied by spatially widespread changes in intrinsic oscillatory dynamics and excitability. *Neuron* 56: 1061–1075, 2007. doi:10.1016/j.neuron.2007.10.033.

Narayanan R, Johnston D. The h channel mediates location dependence and plasticity of intrinsic phase response in rat hippocampal neurons. *J Neurosci* 28: 5846–5860, 2008. doi:10.1523/JNEUROSCI.0835-08.2008.

Narayanan R, Johnston D. The h current is a candidate mechanism for regulating the sliding modification threshold in a BCM-like synaptic learning rule. *J Neurophysiol* 104: 1020–1033, 2010. doi:10.1152/jn.01129.2009.

Neunuebel JP, Knierim JJ. CA3 retrieves coherent representations from degraded input: direct evidence for CA3 pattern completion and dentate

gyrus pattern separation. *Neuron* 81: 416–427, 2014. doi:10.1016/j.neuron.2013.11.017.

Nolan MF, Malleret G, Dudman JT, Buhl DL, Santoro B, Gibbs E, Vronskaya S, Buzsáki G, Siegelbaum SA, Kandel ER, Morozov A. A behavioral role for dendritic integration: HCN1 channels constrain spatial memory and plasticity at inputs to distal dendrites of CA1 pyramidal neurons. *Cell* 119: 719–732, 2004. doi:10.1016/j.cell.2004.11.020.

Nusser Z. Variability in the subcellular distribution of ion channels increases neuronal diversity. *Trends Neurosci* 32: 267–274, 2009. doi:10.1016/j.tins.2009.01.003.

Padmanabhan K, Urban NN. Intrinsic biophysical diversity decorrelates neuronal firing while increasing information content. *Nat Neurosci* 13: 1276–1282, 2010. doi:10.1038/nn.2630.

Pedroni A, Minh D, Mallamaci A, Cherubini E. Electrophysiological characterization of granule cells in the dentate gyrus immediately after birth. *Front Cell Neurosci* 8: 44, 2014. doi:10.3389/fncel.2014.00044.

Pignatelli M, Ryan TJ, Roy DS, Lovett C, Smith LM, Muralidhar S, Tonegawa S. Engram cell excitability state determines the efficacy of memory retrieval. *Neuron* 101: 274–284.e5, 2019. doi:10.1016/j.neuron.2018.11.029.

Pike FG, Goddard RS, Suckling JM, Ganter P, Kasthuri N, Paulsen O. Distinct frequency preferences of different types of rat hippocampal neurones in response to oscillatory input currents. *J Physiol* 529: 205–213, 2000. doi:10.1111/j.1469-7793.2000.00205.x.

Prescott SA, De Koninck Y, Sejnowski TJ. Biophysical basis for three distinct dynamical mechanisms of action potential initiation. *PLOS Comput Biol* 4: e1000198, 2008a. doi:10.1371/journal.pcbi.1000198.

Prescott SA, Ratté S, De Koninck Y, Sejnowski TJ. Nonlinear interaction between shunting and adaptation controls a switch between integration and coincidence detection in pyramidal neurons. *J Neurosci* 26: 9084–9097, 2006. doi:10.1523/JNEUROSCI.1388-06.2006.

Prescott SA, Ratté S, De Koninck Y, Sejnowski TJ. Pyramidal neurons switch from integrators in vitro to resonators under in vivo-like conditions. *J Neurophysiol* 100: 3030–3042, 2008b. doi:10.1152/jn.90634.2008.

Prinz AA, Bucher D, Marder E. Similar network activity from disparate circuit parameters. *Nat Neurosci* 7: 1345–1352, 2004. doi:10.1038/nn1352.

Ramirez-Amaya V, Angulo-Perkins A, Chawla MK, Barnes CA, Rosi S. Sustained transcription of the immediate early gene Arc in the dentate gyrus after spatial exploration. *J Neurosci* 33: 1631–1639, 2013. doi:10.1523/JNEUROSCI.2916-12.2013.

Ramirez-Amaya V, Marrone DF, Gage FH, Worley PF, Barnes CA. Integration of new neurons into functional neural networks. *J Neurosci* 26: 12237–12241, 2006. doi:10.1523/JNEUROSCI.2195-06.2006.

Ramírez-Amaya V, Vazdarjanova A, Mikhael D, Rosi S, Worley PF, Barnes CA. Spatial exploration-induced Arc mRNA and protein expression: evidence for selective, network-specific reactivation. *J Neurosci* 25: 1761–1768, 2005. doi:10.1523/JNEUROSCI.4342-04.2005.

Rathour RK, Malik R, Narayanan R. Transient potassium channels augment degeneracy in hippocampal active dendritic spectral tuning. *Sci Rep* 6: 24678, 2016. doi:10.1038/srep24678.

Rathour RK, Narayanan R. Inactivating ion channels augment robustness of subthreshold intrinsic response dynamics to parametric variability in hippocampal model neurons. *J Physiol* 590: 5629–5652, 2012a. doi:10.1113/jphysiol.2012.239418.

Rathour RK, Narayanan R. Influence fields: a quantitative framework for representation and analysis of active dendrites. *J Neurophysiol* 107: 2313–2334, 2012b. doi:10.1152/jn.00846.2011.

Rathour RK, Narayanan R. Homeostasis of functional maps in active dendrites emerges in the absence of individual channelostasis. *Proc Natl Acad Sci USA* 111: E1787–E1796, 2014. doi:10.1073/pnas.1316599111.

Rathour RK, Narayanan R. Degeneracy in hippocampal physiology and plasticity. *Hippocampus* 29: 980–1022, 2019. doi:10.1002/hipo.23139.

Ratté S, Hong S, De Schutter E, Prescott SA. Impact of neuronal properties on network coding: roles of spike initiation dynamics and robust synchrony transfer. *Neuron* 78: 758–772, 2013. doi:10.1016/j.neuron.2013.05.030.

Renart A, Song P, Wang XJ. Robust spatial working memory through homeostatic synaptic scaling in heterogeneous cortical networks. *Neuron* 38: 473–485, 2003. doi:10.1016/S0896-6273(03)00255-1.

Sabah NH, Leibovic KN. Subthreshold oscillatory responses of the Hodgkin-Huxley cable model for the squid giant axon. *Biophys J* 9: 1206–1222, 1969. doi:10.1016/S0006-3495(69)86446-5.

Sahay A, Wilson DA, Hen R. Pattern separation: a common function for new neurons in hippocampus and olfactory bulb. *Neuron* 70: 582–588, 2011. doi:10.1016/j.neuron.2011.05.012.

Sainsbury RS, Bland BH. The effects of selective septal lesions on theta production in CA1 and the dentate gyrus of the hippocampus. *Physiol Behav* 26: 1097–1101, 1981. doi:10.1016/0031-9384(81)90214-6.

Satvat E, Gheidi A, Voll S, Odintsova IV, Marrone DF. Location is everything: neurons born during fluoxetine treatment accumulate in regions that do not support spatial learning. *Neuropharmacology* 62: 1627–1633, 2012. doi:10.1016/j.neuropharm.2011.11.025.

Schmidt-Hieber C, Jonas P, Bischofberger J. Enhanced synaptic plasticity in newly generated granule cells of the adult hippocampus. *Nature* 429: 184–187, 2004. doi:10.1038/nature02553.

Schmidt-Hieber C, Jonas P, Bischofberger J. Subthreshold dendritic signal processing and coincidence detection in dentate gyrus granule cells. *J Neurosci* 27: 8430–8441, 2007. doi:10.1523/JNEUROSCI.1787-07.2007.

Schneider CJ, Cuntz H, Soltesz I. Linking macroscopic with microscopic neuroanatomy using synthetic neuronal populations. *PLOS Comput Biol* 10: e1003921, 2014. doi:10.1371/journal.pcbi.1003921.

Sehgal M, Song C, Ehlers VL, Moyer JR. Learning to learn—intrinsic plasticity as a metaplasticity mechanism for memory formation. *Neurobiol Learn Mem* 105: 186–199, 2013. doi:10.1016/j.nlm.2013.07.008.

Senzai Y, Buzsáki G. Physiological properties and behavioral correlates of hippocampal granule cells and mossy cells. *Neuron* 93: 691–704.e5, 2017. doi:10.1016/j.neuron.2016.12.011.

Seress L, Pokorny J. Structure of the granular layer of the rat dentate gyrus. A light microscopic and Golgi study. *J Anat* 133: 181–195, 1981.

Shamir M, Sompolinsky H. Implications of neuronal diversity on population coding. *Neural Comput* 18: 1951–1986, 2006. doi:10.1162/neco.2006.18.8.1951.

Silva AJ, Zhou Y, Rogerson T, Shobe J, Balaji J. Molecular and cellular approaches to memory allocation in neural circuits. *Science* 326: 391–395, 2009. doi:10.1126/science.1174519.

Sjöström PJ, Häusser M. A cooperative switch determines the sign of synaptic plasticity in distal dendrites of neocortical pyramidal neurons. *Neuron* 51: 227–238, 2006. doi:10.1016/j.neuron.2006.06.017.

Soltesz I, Losonczy A. CA1 pyramidal cell diversity enabling parallel information processing in the hippocampus. *Nat Neurosci* 21: 484–493, 2018. doi:10.1038/s41593-018-0118-0.

Srikanth S, Narayanan R. Variability in state-dependent plasticity of intrinsic properties during cell-autonomous self-regulation of calcium homeostasis in hippocampal model Neurons. *eNeuro* 2: ENEURO.0053-0015.2015, 2015. doi:10.1523/ENEURO.0053-15.2015.

Staley KJ, Otis TS, Mody I. Membrane properties of dentate gyrus granule cells: comparison of sharp microelectrode and whole-cell recordings. *J Neurophysiol* 67: 1346–1358, 1992. doi:10.1152/jn.1992.67.5.1346.

Stegen M, Kirchheim F, Hanuschkin A, Staszewski O, Veh RW, Wolfart J. Adaptive intrinsic plasticity in human dentate gyrus granule cells during temporal lobe epilepsy. *Cereb Cortex* 22: 2087–2101, 2012. doi:10.1093/cercor/bhr294.

Strange BA, Witter MP, Lein ES, Moser EI. Functional organization of the hippocampal longitudinal axis. *Nat Rev Neurosci* 15: 655–669, 2014. doi:10.1038/nrn3785.

Surges R, Kukley M, Brewster A, Rüschenschmidt C, Schramm J, Baram TZ, Beck H, Dietrich D. Hyperpolarization-activated cation current I_h of dentate gyrus granule cells is upregulated in human and rat temporal lobe epilepsy. *Biochem Biophys Res Commun* 420: 156–160, 2012. doi:10.1016/j.bbrc.2012.02.133.

Tikidji-Hamburyan RA, Martínez JJ, White JA, Canavier CC. Resonant interneurons can increase robustness of gamma oscillations. *J Neurosci* 35: 15682–15695, 2015. doi:10.1523/JNEUROSCI.2601-15.2015.

Titley HK, Brunel N, Hansel C. Toward a neurocentric view of learning. *Neuron* 95: 19–32, 2017. doi:10.1016/j.neuron.2017.05.021.

Tonegawa S, Morrissey MD, Kitamura T. The role of engram cells in the systems consolidation of memory. *Nat Rev Neurosci* 19: 485–498, 2018. doi:10.1038/s41583-018-0031-2.

Tripathy SJ, Padmanabhan K, Gerkin RC, Urban NN. Intermediate intrinsic diversity enhances neural population coding. *Proc Natl Acad Sci USA* 110: 8248–8253, 2013. doi:10.1073/pnas.1221214110.

Valero M, Cid E, Averkin RG, Aguilar J, Sanchez-Aguilera A, Viney TJ, Gomez-Dominguez D, Bellistri E, de la Prida LM. Determinants of different deep and superficial CA1 pyramidal cell dynamics during sharp-wave ripples. *Nat Neurosci* 18: 1281–1290, 2015. doi:10.1038/nn.4074.

van Praag H, Schinder AF, Christie BR, Toni N, Palmer TD, Gage FH. Functional neurogenesis in the adult hippocampus. *Nature* 415: 1030–1034, 2002. doi:10.1038/4151030a.

Voliotis M, Perrett RM, McWilliams C, McArdle CA, Bowsher CG. Information transfer by leaky, heterogeneous, protein kinase signaling systems. *Proc Natl Acad Sci USA* 111: E326–E333, 2014. doi:10.1073/pnas.1314446111.

Wang XJ, Buzsáki G. Gamma oscillation by synaptic inhibition in a hippocampal interneuronal network model. *J Neurosci* 16: 6402–6413, 1996. doi:10.1523/JNEUROSCI.16-20-06402.1996.

Watanabe S, Hoffman DA, Migliore M, Johnston D. Dendritic K^+ channels contribute to spike-timing dependent long-term potentiation in hippocampal pyramidal neurons. *Proc Natl Acad Sci USA* 99: 8366–8371, 2002. doi:10.1073/pnas.122210599.

Williams PA, Larimer P, Gao Y, Strowbridge BW. Semilunar granule cells: glutamatergic neurons in the rat dentate gyrus with axon collaterals in the inner molecular layer. *J Neurosci* 27: 13756–13761, 2007. doi:10.1523/JNEUROSCI.4053-07.2007.

Winson J. Patterns of hippocampal theta rhythm in the freely moving rat. *Electroencephalogr Clin Neurophysiol* 36: 291–301, 1974. doi:10.1016/0013-4694(74)90171-0.

Winson J. Loss of hippocampal theta rhythm results in spatial memory deficit in the rat. *Science* 201: 160–163, 1978. doi:10.1126/science.663646.

Yiu AP, Mercaldo V, Yan C, Richards B, Rashid AJ, Hsiang HL, Pressey J, Mahadevan V, Tran MM, Kushner SA, Woodin MA, Frankland PW, Josselyn SA. Neurons are recruited to a memory trace based on relative neuronal excitability immediately before training. *Neuron* 83: 722–735, 2014. doi:10.1016/j.neuron.2014.07.017.

Zemankovics R, Káli S, Paulsen O, Freund TF, Hájos N. Differences in subthreshold resonance of hippocampal pyramidal cells and interneurons: the role of h-current and passive membrane characteristics. *J Physiol* 588: 2109–2132, 2010. doi:10.1113/jphysiol.2009.185975.

Zhou P, Burton SD, Urban NN, Ermentrout GB. Impact of neuronal heterogeneity on correlated colored noise-induced synchronization. *Front Comput Neurosci* 7: 113, 2013. doi:10.3389/fncom.2013.00113.

Zhou Y, Won J, Karlsson MG, Zhou M, Rogerson T, Balaji J, Neve R, Poirazi P, Silva AJ. CREB regulates excitability and the allocation of memory to subsets of neurons in the amygdala. *Nat Neurosci* 12: 1438–1443, 2009. doi:10.1038/nn.2405.